Icarus 409 (2024) 115862

Contents lists available at ScienceDirect

Icarus

journal homepage: www.elsevier.com/locate/icarus

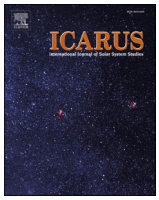

H_2CO, O_3, NH_3, HCN, N_2O, NO_2, NO, and HO_2 upper limits of detection in the Venus lower-mesosphere using SOIR on board Venus Express

A. Mahieux [a,b,*], S. Viscardy [a], K.L. Jessup [c], F.P. Mills [b,d,e], L. Trompet [a], S. Robert [a], S. Aoki [a,f], A. Piccialli [a], A.C. Vandaele [a]

[a] Royal Belgian Institute for Space Aeronomy, Brussels, Belgium
[b] The University of Texas at Austin, Austin, TX, United States
[c] South West Research Institute, Boulder, CO, United States
[d] Space Science Institute, Boulder, CO, United States
[e] The Australian National University, Canberra, ACT, Australia
[f] The University of Tokyo, Tokyo, Japan

ARTICLE INFO

Keywords:
Venus mesosphere
Minor species
Upper limits values

ABSTRACT

We report on mean upper limit number densities and volume concentrations of H_2CO, O_3, NH_3, HCN, N_2O, NO_2, NO, and HO_2 at the Venus terminator above the cloud layer, computed from the SOIR/Venus Express transmittances measured during hundreds of solar occultations. An unsuccessful attempt to detect these species using the statistical algorithm described in Mahieux et al. (2023a) is reported, and upper limits of detection using the method presented by Trompet et al. (2021) are provided.

The mean upper limit volume mixing ratios at an altitude of ~80 km at the Venus terminator are equal to 43 ± 6 ppb ppt for H_2CO, 3.76 ± 5.7 ppm for O_3, 0.69 ± 0.28 ppm for NH_3, 38.3 ± 7.9 ppm for HCN, 0.14 ± 0.02 ppm for N_2O, 0.47 ± 0.32 ppm for NO_2, 6.15 ± 1.84 ppm for NO, and 99.5 ± 62.2 ppb for HO_2.

1. Introduction

The Venus upper-mesosphere, located between the cloud layer and the thermosphere (~65 km – 120 km), was a barely known region of the Venus atmosphere that has been revealed thanks to the European mission Venus Express (VEx, 2006–2014) (Titov et al., 2006a). On board the spacecraft were several spectrometers such as SOIR (Mahieux et al., 2008), SPICAV (Bertaux et al., 2007), and VIRTIS (Piccioni et al., 2007), all working in nadir, solar, and/or stellar occultation modes, VeRa (Häusler et al., 2006) performing radio Earth-occultations, and VMC (Markiewicz et al., 2007), a multispectral camera. These instruments provided a large dataset regarding the Venus atmosphere composition (Gilli et al., 2015; Royer et al., 2016; Vandaele et al., 2016a; Belyaev et al., 2017; Marcq et al., 2018; Marcq et al., 2019; Marcq et al., 2020; Evdokimova et al., 2021; Oschlisniok et al., 2021; Mahieux et al., 2023a), thermal structure (Tellmann et al., 2012; Mahieux et al., 2015a; Piccialli et al., 2015; Limaye et al., 2017; Limaye et al., 2018), and dynamical activity (Piccialli et al., 2012; Khatuntsev et al., 2013; Piccialli et al., 2014; Müller-Wodarg et al., 2016).

Its bulk composition is dominated by CO_2 (96.5%) and N_2 (3.5%). However, in the upper atmosphere, CO_2 is gradually replaced with increasing altitude by CO and atomic O, produced by its photolysis. Many other minor species were detected, including CO (Vandaele et al., 2015; Vandaele et al., 2016b; Mahieux et al., 2023b), H_2O and HDO (Fedorova et al., 2008; Chamberlain et al., 2020; Mahieux et al., 2023b), HCl and HF (Mahieux et al., 2015c; Mahieux et al., 2023b), SO_2 (Mahieux et al., 2015b; Evdokimova et al., 2021; Mahieux et al., 2023a), O_3 (Montmessin et al., 2011; Marcq et al., 2019; Evdokimova et al., 2021), OCS (Marcq et al., 2018; Mahieux et al., 2023a), and more recently SO_3, CS, and CS_2 (Mahieux et al., 2023a). Krasnopolsky (2006) reported ground-based telescope detections of nitrogen monoxide (NO) at the cloud top, which could indicate the occurrence of lightning within the Venus clouds. Hydroxyl (OH) was also detected in the VIRTIS/VEx spectra (Piccioni et al., 2008). From photochemical models, many other species are expected to be present in the Venus mesosphere due to their roles in the putative carbon and sulfur cycles; see, for example, Mills and Allen (2007); Mills et al. (2007); Zhang et al. (2012).

Recently, Greaves et al. (2021); Greaves et al. (2023) reported detections of phosphine (PH_3). This discovery would imply the presence of redox disequilibrium in the clouds, and its existence, together with that

* Corresponding author at: Royal Belgian Institute for Space Aeronomy, Brussels, Belgium.
E-mail address: arnaud.mahieux@aeronomie.be (A. Mahieux).

https://doi.org/10.1016/j.icarus.2023.115862
Received 26 July 2023; Received in revised form 5 October 2023; Accepted 6 November 2023
Available online 10 November 2023

of ammonia (NH_3), was suggested as a potential indication of biological anomalies (Bains et al., 2021; Cleland and Rimmer, 2022). However, these PH_3 detections have been met with strong opposition from an independent reanalysis of the data (Villanueva et al., 2021), as well as by other ground-based telescope observations (Encrenaz et al., 2020) and solar occultations conducted by SOIR/VEx, which led to stringent upper limits on the PH_3 concentration above the cloud top (Trompet et al. (2021).

Similarly, there have been reports of tentative of NH_3 detections in the cloud layer by the Venera 8 chemical probe (Surkov et al., 1973; Zolotov, 1991), as well as a reanalysis of the Pioneer Venus (PV) Large Probe Neutral Mass Spectrometer (LPNMS) dataset, which also suggested the presence of NH_3 (Mogul et al., 2021). According to Clements (2022), unpublished ground-based observations have also apparently revealed the presence of NH_3, providing further support for the earlier attempts to detect this compound on Venus. Additionally, in their reanalysis of the LPNMS dataset, Mogul et al. (2021) interpreted signals that could indicate the existence of other nitrogen-bearing species in the clouds, such as HNO_3, HNO_2, NO_2, HNO, NO, NH_2D, NH_2, NH, N, and HCN, but without providing concentrations and associated uncertainties up to date.

In this work, we aim to target a list of nitrogen-, oxygen-, and hydrocarbon-bearing species that have not yet been measured above the cloud layer (besides ozone) but have weak absorption bands in the mid-IR (2.2–4.4 μm), using the SOIR/VEx transmittance spectra and a statistical technique that was used in Mahieux et al. (2023a) to detect SO_2, SO_3, OCS, CS, and CS_2 above the cloud layer. We could not report on the positive detection of any new species but rather provide the upper limits of detection for H_2CO, O_3, NH_3, HCN, N_2O, NO_2, NO, and HO_2 using the technique presented in Trompet et al. (2021).

Section 2 describes the SOIR instrument and Section 3 the spectroscopy of the targeted species in the near-IR sounded by SOIR. Section 4 presents the upper limit computations, and Section 5 discusses the retrieval algorithm and its expected performances; an example of non-detection is also provided in Section 6 for H_2CO. The number density and volume mixing ratio profiles of all species' upper limits are provided and discussed in Section 7. The conclusions are given in Section 8.

2. The SOIR instrument

The SOIR instrument was an infrared echelle grating spectrometer on board the ESA Venus Express (VEx) spacecraft, which orbited Venus from May 2006 until December 2014 (Titov et al., 2006b). The VEx spacecraft was on an elliptical orbit around Venus, with its perigee above the North Pole at an altitude of ~250 to 500 km and its apogee above the South Pole between 45,000 and 65,000 km. SOIR was exclusively working in solar occultation mode, i.e., only taking measurements at 6 AM or 6 PM local solar time (LST) and covering all latitudes from Pole to Pole. It measured transmittance spectra above the cloud layer, at altitudes ranging from 65 to 170 km.

SOIR was sensitive from 2.2 to 4.4 μm (2200–4400 cm^{-1}) (Mahieux et al., 2008), recording spectra in small spectral regions (with a spectral width of ~24 cm^{-1}) corresponding to the echelle diffraction orders (ranging from 101 to 194), called orders hereafter. The detector comprised 320 pixels in its spectral direction and 256 pixels in its spatial direction, of which 24 rows were illuminated. Because of telemetry limitations, only two rows of spectral data could be sent back to Earth, forcing the data to be combined into two bins on board the spacecraft. The projections of the two bins at the tangent point were located at two slightly different altitude levels.

An Acousto Optical Tunable Filter (AOTF) was placed right after the entrance optics to select the central order to be measured. The AOTF had a transfer function (TF) with a shape close to a $sinc^2$ and modelled as a sum of $sinc^2$ whose central lobe full width at half maximum (FWHM) was equal to ~24 cm^{-1}, and side lobes extending up to 80 cm^{-1} from the centre of the main lobe (Mahieux et al., 2009). The instrument's free spectral range was equal to 24 cm^{-1}. Therefore, when measuring a spectrum, SOIR recorded absorption structures from the central order and the three orders just above and below, all modulated by the AOTF TF. The AOTF was driven by radio frequency (RF) to select the location of the $sinc^2$-like function. A second-order polynomial expression gives the relationship between AOTF maximum and RF (Mahieux et al., 2008).

During a solar occultation, the spacecraft was set in an inertial mode such that the SOIR entrance slit would always point at the Sun. The Sun disk fully covered the entrance slit of the instrument. During an occultation, SOIR was first measuring free of atmosphere raw spectra (in an ingress configuration), for which the minimum altitude of the line of sight was larger than 220 km, followed by atmospheric raw spectra, for which the tangent altitude was comprised between 220 and 60 km. The free-of-atmosphere raw spectra were measured in the egress configuration after the atmospheric raw spectra. The transmittance spectra and the associated noise were computed by dividing the atmospheric raw spectra by the atmosphere-free raw spectra, following a procedure described by Vandaele et al. (2013) and Trompet et al. (2016). The solar occultation technique is powerful because it does not require radiometric calibrations since the products are self-calibrated transmittance spectra and only need spectral calibration. SOIR could target four different orders during an occultation, each measured at a 1 Hz cadence, thus providing eight independent sets of transmittance spectra, two for each order corresponding to the two spatial bins.

The signal-to-noise ratio (SNR) varied between 500 and 3000 (Vandaele et al., 2013; Trompet et al., 2016); a short summary on the spectral noise computation is provided in Section 4. The spectral resolution ranged between 0.11 and 0.21 cm^{-1} ($R = \frac{\lambda}{\Delta\lambda} \approx 21,000$), while the spectral width of a pixel varied between 0.06 and 0.12 cm^{-1}, both with increasing order. The pixel-to-wavenumber calibration was computed using a fourth-order polynomial, accounting for the Doppler shift of the spectral lines due to the relative speed of VEx relative to Venus; in some cases, the Doppler shift could be larger than a pixel spectral width (Mahieux et al., 2008). The vertical spatial resolution of the instrument, which includes the combined effects of the projection of half of the slit at the tangent point and the smearing due to the spacecraft movement during the time of a spectrum acquisition, stretched from 200 m for North polar observations to 5 km at the South Pole. The vertical sampling distance, the vertical distance between two successive observations, was also latitude dependent, varying between 2 km for North polar observations, 500 m at latitudes between 40° and 70°N, and 5 km in the South polar region.

During the eight years of instrument operation, nearly 1500 occultations were performed, recording >200,000 atmospheric spectra.

3. Spectroscopy

The species targeted in this work all have intensities multiplied by expected abundances that are very close to the detection limit of SOIR. They are spread over the entire spectral range, see Fig. 1, where the position and intensity of all the expected species multiplied by typical volume mixing ratios (VMR, see legend of the figure) at 80 km are depicted. The orders in which H_2CO, O_3, NH_3, HCN, N_2O, NO_2, NO, and HO_2 absorb are also listed in Table 1.

Appendix A provides the list of rovibrational bands for all the species fitted in each order.

We note that, for NH_3 and NO in Table 1, not all the transitions are listed because their IR rovibrational HITRAN are numerous, and their notations are not as simplistic as for the other species.

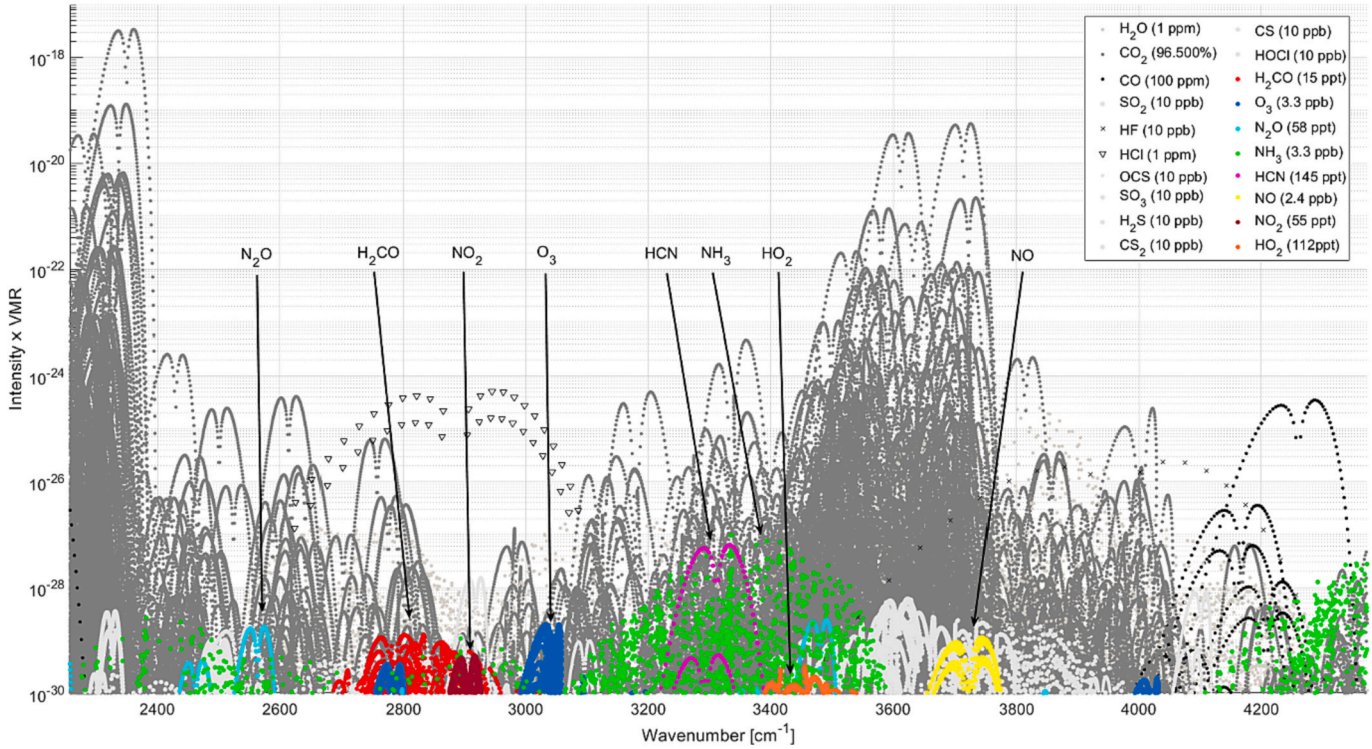

Fig. 1. Positions and line intensities multiplied by typical VMRs at 80 km (see legend) of all the species absorbing in the Venus atmosphere in grey and those targeted in this work in colours. The spectral information is taken from HITRAN (Gordon et al., 2017). The species targeted in Mahieux et al. (2023a) are displayed as light grey markers.

4. Upper limit computation

4.1. Computation of the SOIR noise

The uncertainties on the spectra are computed as described in Vandaele et al. (2013): the uncertainties δP are computed individually for each pixel of each spectra of the atmosphere

$$\delta P = \delta U + \sqrt{T}(\delta S - \delta U) \quad (1)$$

where $T = \frac{U}{S}$ is the transmittance value, δS is the standard deviation over the Sun spectra (mainly Poisson noise) for one pixel and δU is the standard deviation for one pixel over the spectra measured while pointing to Venus (umbra - mainly background noise). The definition of the Sun, atmospheric, and umbra spectra are defined in Vandaele et al. (2013) and Trompet et al. (2016). The raw spectra are corrected pixel-by-pixel for raw signal drifts observed in the Sun spectra S.

The uncertainties on the transmittance spectra δT are computed from

$$\delta T = \frac{\sqrt{\delta P^2 + T2\delta S2}}{S} \quad (2)$$

where S is the extrapolated Sun spectrum into the atmosphere (see Trompet et al., 2016).

The pixel-to-pixel variability in terms of photons when observing white source is not accounted for since it cancels out when computing the transmittances, and is provided in Mahieux et al. (2008).

The upper limits are computed using the algorithm described in Appendix F of Trompet et al. (2021), which was used to confirm no detection of phosphine in the SOIR spectra.

The upper limit computation method relies mostly on the computation of the noise level of the SOIR observation (Trompet et al., 2016), which includes the photon random noise and the other noise sources such as the drifts of the raw signal with time. We refer the reader to Trompet et al. (2016) for a detailed description of the procedures to compute the SOIR noise level; a short summary is provided in Section 4.

In that method, the SOIR measurement altitudes and the corresponding transmittance uncertainties are considered one by one. For each measurement altitude z_i in a given order, assuming a constant VMR with altitude of targeted species X, the optical depth $\tau_X(z_i)$ from the top of the atmosphere (taken here as 190 km) down to measurement altitude is computed, considering all the species absorbing in the order, the AOTF TF, and the order addition procedure described in Section 2, and convolved to the SOIR spectral resolution. Separately, the SOIR spectral uncertainties on the measured transmittances are inverted into equivalent optical depths $\tau_{err}(z_i)$ using relation (F.2) from Trompet et al. (2021), which considers the measured spectral uncertainties, the background transmittance level, and the ratio between the contributions from the central order radiance and the total radiance obtained when probing the measurement altitude. In the relation provided in the paper, a factor 3.2 to the noise level appears, to decipher between white noise detections and clear detections, as recommended by IUPAC (IUPAC, 2008). The two optical depths are compared and the minimum over the order spectral range determines the targeted species X upper limit VMR at altitude z_i.

The error on the upper limit is computed considering the uncertainty on the background transmittance level in relation (F.2) of Trompet et al. (2021).

5. Retrieval algorithm

We use in this work the same retrieval algorithm as in Mahieux et al. (2023a), which was designed to retrieve sulfur minor species (SO_2, SO_3, OCS, CS, and CS_2). These species also have spectral signature close to the SOIR noise level, and statistical criteria were designed to differentiate between detections and upper limit values.

For a given solar occultation on a given order and a given bin, we consider the transmittance spectra measured between tangent altitudes of 60–100 km with a mean transmittance larger than 0.01 and their

Table 1
List of the SOIR orders considered in this work, their theoretical spectral extents, the targeted species and their vibrational transitions in HITRAN notations (Gordon et al., 2017), and the other species absorbing in the order. The minor species listed in the last column were targeted in Mahieux et al. (2023a).

Order	Wavenumber range [cm^{-1}]	Targeted species	Targeted vibrational transitions	Major species absorbing in the order	Other minor species absorbing in the order
113	2525.3–2547.0	N_2O	2000–0000	CO_2	CS
114	2547.7–2569.6	N_2O	2000–0000	CO_2, H_2O	
115	2570.0–2592.1	N_2O	2000–0000	CO_2, H_2O	
123	2748.8–2772.4	H_2CO	100,000–000000	CO_2, H_2O, HCl	
124	2771.2–2795.0	H_2CO	100,000–000000 000010–000000	CO_2, H_2O, HCl	SO_3
125	2793.5–2817.5	H_2CO	100,000–000000 000010–000000	CO_2, H_2O, HCl	SO_3
126	2815.9–2840.1	H_2CO	100,000–000000 000010–000000	CO_2, H_2O, HCl	SO_3, CS_2
127	2838.2–2862.6	H_2CO	100,000–000000 000010–000000	CO_2, H_2O, HCl	CS_2
128	2860.6–2885.1	H_2CO	000010–000000	CO_2, H_2O, HCl	OCS
129	2882.9–2907.7	NO_2	101–000 111–010	H_2O, HCl	OCS
130	2905.3–2930.2	NO_2	101–000 111–010	H_2O, HCl	OCS
134	2994.6–3020.4	O_3	003–000	CO_2, H_2O, HCl	
135	3017.0–3042.9	O_3	003–000	CO_2, H_2O, HCl	
145	3240.5–3268.3	HCN	1000–0000	CO_2, H_2O	
146	3262.8–3290.9	HCN	1000–0000	CO_2, H_2O	
147	3285.2–3313.4	HCN	1000–0000	CO_2, H_2O	
148	3307.5–3335.9	HCN	1000–0000	CO_2, H_2O	
149	3329.9–3358.5	HCN	1000–0000	CO_2	
150	3352.2–3381.0	NH_3 HO_2	All transitions 100–000	CO_2, H_2O	
151	3374.6–3403.6	NH_3 HO_2	All transitions 100–000	CO_2, H_2O	
152	3396.9–3426.1	NH_3 HO_2	All transitions 100–000	CO_2, H_2O	
169	3776.8–3809.3	NO	All transitions	CO_2, H_2O	H_2S
170	3799.2–3831.8	NO	All transitions	CO_2, H_2O, HF	H_2S
171	3821.5–3854.4	NO	All transitions	CO_2, H_2O, HF	H_2S
172	3843.9–3876.9	NO	All transitions	CO_2, H_2O	H_2S
173	3866.2–3899.4	NO	All transitions	CO_2, H_2O	H_2S
191	4268.5–4305.2	NH_3	All transitions	CO_2, H_2O, CO, HF	
192	4290.8–4327.7	NH_3	All transitions	CO_2, H_2O, CO, HF	

associated uncertainties. Each spectrum is fitted independently from each other. We use the Levenberg-Marquardt (LM) algorithm to adjust several atmospheric and instrumental parameters, minimising the reduced-χ^2 between the measured spectrum and a synthetic spectrum, weighted by the uncertainty on the measured spectrum. The fitted atmospheric variables are the slant number densities of the targeted species and the other species absorbing in the order (see Table 1), the spectral baseline modelled as a fifth-order polynomial, and a temperature proxy representing the slant mean temperature. Some instrumental parameters are also adjusted. The fitted slant densities are converted into local number densities using the Tikhonov regularisation algorithm (Gröller et al., 2018; Trompet et al., 2023), with the λ-parameter set to 10^{-5}, or 1 when stronger smoothing is required.

Then, the number densities are compared to detection criteria to decide whether a positive detection is found or if only an upper limit is obtained. We use the same four detection statistical criteria as in Mahieux et al. (2023a):

(a) *Detection criterion based on the χ^2 of the fit with and without the targeted minor species.* We run two independent fits on each spectrum: the first one considers all species absorbing in the order (S_1), while the second one only considers the major species (see Table 1) and the non-targeted minor species (S_2). We also build a third spectrum S_3, which considers all the retrieved slant densities retrieved to build S_1, but in which the slant density of the targeted species is set to zero. We then compare the reduced-χ^2 (called simply χ^2 hereafter) of S_1 and S_3, and similar to what was done by Evdokimova et al. (2021), we decide that the criterion is satisfied if it lowers by at least 5%. We categorise the detections when the χ^2 lowers by 5%, 10%, or 20%. We also impose χ^2 from S_1 to be smaller than χ^2 of S_2 by the same amount.

(b) *Detection criterion based on the detection upper limit.* For each fitted spectrum, we compute the upper limit of detection, using the relationships provided in Appendix F of Trompet et al. (2021) and described in the previous Section, by comparing the noise in the measured spectrum with the targeted species absorption cross-section. If the retrieved slant density is larger than the detection upper limit by at least a factor 1, a white-noise detection can be claimed; if the retrieved slant density is larger by a factor 3.2, a clear detection can be claimed.

(c) *Detection criterion based on the correlation of the spectra.* We compute the correlation coefficients between the measured spectrum M and S_1, S_2, and S_3. This criterion is satisfied only if the correlation between the measured spectrum and S_1 is larger than the correlation between the measured spectrum and S_2. The same criterion is used between M and S_3.

(d) *Detection criterion on the uncertainties of the retrieved slant densities.* Only retrieved slant densities that have relative uncertainties lower than unity are considered.

Detections are claimed if all four detection criteria defined above are satisfied.

Even though the LM fit is done on the whole measured spectra, the criteria above are applied only on the regions where the SOIR transmittances are the best, i.e., discarding the wavenumber regions corresponding to detector pixels 1 to 100 and 300 to 320, and for some species on the regions where the targeted species have strong enough absorption lines to be detected, ignoring the other spectral regions; see Table 2.

Table 2
List of the intervals, by species and order, on which the criteria are used to decide for a detection.

Species	Order	Intervals [cm^{-1}]
N_2O	113	2532–2545.7
	114	2554.4–2562
	115	2576.8–2588
H_2CO	123	2756–2770.9
	124	2778.4–2782
	125	2800.8–2816
	126	2823.2–2838.5
	127	2845.6–2861.1
	128	2868.1–2883.6
NO_2	129	2890.5–2900
	130	2912.9–2925
O_3	134	3002.5–3018.8
	135	3025–3041.3
HCN	145	3251.4–3252.6, 3258–3259, 3261–3262, 3264.5–3265.5
	146	3276.8–3278.5, 3280.5–3281.5, 3283.4–3284.6, 3283.8–3284.6, 3286.8–3287.8
	147	3296–3297, 3299–3300, 3305–3306
	148	3319.5–3321, 3325.5–3326.5, 3328.4–3329.2, 3331–3332
	149	3339.5–3340.5, 3342–3343, 3345–3346, 3347.5–3348.5, 3350–3351, 3352.5–3354.5
	150	3366–3372, 3374–3378
NH_3	151	3390–3400
	152	3412–3417
	191	4287–4294
	192	4310–4320
NO	169	3786.7–3807.2
	170	3809–3810, 3812–3813, 3821.5–3823
	171	3831.5–3846
	172	3853.9–3874.8
	173	3876.4–3897.3
HO_2	150	3361–3379.2
	151	3387–3403
	152	3414–3418

Similar to what was done in Mahieux et al. (2023a), the performances of the algorithm are checked on synthetic spectra, built using known local number densities of the absorbing species and adding random noise with different SNRs equal to 500, 1000, 2000, and 3000. The study is provided in Appendix B.

6. Example of non-detection

To illustrate the two approaches described in the two previous Sections, we present here the unsuccessful attempt to detect H_2CO in occultation 1034.1 measured on 18 February 2009 at a latitude of 84°N and longitude of 111°W on the morning side of the terminator. Orders 123, 124, and 125 were recorded during that observation, where H_2CO absorb.

These orders record the absorption structures of CO_2, HCl, H_2O, and H_2CO. H_2CO was not detected at any altitude level under the conditions described in Section 5.

We consider, as an illustrative example, the spectrum taken at an altitude of 71 km in order 125 bin #1.

The retrieval attempt is plotted in Fig. 2A, where the measured spectrum, the best fit of the major and minor species (Simulation S_1, considering $CO_2 + HCl + H_2O + H_2CO$) synthetic spectrum, the best fit of the major species only and non-targeted minor species (Simulation S_2, considering $CO_2 + HCl + H_2O$) synthetic spectrum, and the best fit of the major and minor species from which the signature of the targeted minor species H_2CO is set to zero (Simulation S_3, considering (CO_2 + HCl + H_2O + H_2CO) – (H_2CO)) are plotted. M refers to the measured transmittance, and dM to the noise. The black shaded region corresponds to the spectral region that is not considered while using the criteria described in Section 5. The correlation coefficients between the measured spectrum M and the synthetic spectra are given in the legend.

In Fig. 2B, we provide the noise level, the H_2CO signature (given as S_1–S_3) as the black spectrum, and the residuals of (M–S_1), (M–S_2), and (M–S_3). The χ^2_ν are given in the legend. We note that in most of the spectral regions where H_2CO has a stronger signature, the fit is enhanced; however, the H_2CO signature never exceeds the noise level. This justifies the fact that no detection was claimed for this particular fit. Moreover, even though the χ^2_ν and the correlation coefficients get enhanced while including H_2CO in the fit (comparing $\chi^2_{(M-S_1)}$ and $\chi^2_{(M-S_2)}$), it only decreases by 4.2% (thus less than the minimum 5% set in the previous section). Furthermore, $\chi^2_{(M-S_3)}$ is larger than $\chi^2_{(M-S_1)}$. The correlation coefficient of M with S_1 is smaller than between M and S_2, but larger than the one between M and S_3. Thus, the criterions defined in Section 5 are not fulfilled.

Fig. 2C shows the residuals divided by the noise level, which are used to compute the χ^2_ν.

We also present in Fig. 2D and E the histograms of the distributions of the weighted residuals relative to the two fits, $H_{(M-S_1)}$ and $H_{(M-S_2)}$, similar to what was done in Mahieux et al. (2023a). We fit a Gaussian to each of those, and compute their σ-values $\sigma_{H_{(M-S_1)}}$ and $\sigma_{H_{(M-S_2)}}$ and the corresponding uncertainties $\delta\sigma_{H_{(M-S_1)}}$ and $\delta\sigma_{H_{(M-S_2)}}$. We see that the σ_H-values are significantly different by 1-σ, since their 1-σ uncertainty intervals do not cover each other: $\sigma_{H_{(M-S_1)}} + \delta\sigma_{H_{(M-S_1)}} < \sigma_{H_{(M-S_2)}} - \delta\sigma_{H_{(M-S_2)}}$ ($4.6107 + 0.1786 > 4.9789 - 0.1791$), even though no detection was claimed.

Finally, we present the upper limit number density profile and the corresponding uncertainties obtained using the method described in Section 4 in Fig. 2F, and the VMR profile and uncertainties in Fig. 2G. The VMR is computed from the simultaneously measured CO_2 number density considering the CO_2 VMR from VIRA (Venus International Reference Atmosphere (Hedin et al., 1983; Zasova et al., 2006)), which is equal to ~96.5% in the considered altitude region. Below 72 km of altitude, the CO_2 could not be retrieved with confidence because of atmospheric saturation of the CO_2 lines (the transmittances computed from the optical depth at atmospheric resolution have values at the peak of the absorption lines lower than 0.15), which explains the sudden increase of the uncertainty in H_2CO upper limit VMR.

7. Results

7.1. Summary of the observations

As already mentioned above, no positive detection of H_2CO, O_3, NH_3, HCN, N_2O, NO_2, NO, nor HO_2 could be obtained using the algorithm described in Section 4, which was used to successfully derive SO_2, SO_3, OCS, CS, and CS_2 in Mahieux et al. (2023a). This means that not all four criteria could be met simultaneously for any spectra in which the targeted species could have absorption structures.

Therefore, we provide the mean upper limit number density and VMR profile for different latitude bins and the whole database separated by side of the terminator, where the observation is sufficiently robust for meaningful interpretation. Hence, we fixed the minimum number of observations to compute a mean profile to 10 (see Table 3). Thus, for those species for which the statistics is not good enough to separate by side of the terminator or by latitude bins, they are not computed. This is the case for ozone, for which the latitude dependence could not be studied for all bins, and for nitrous oxide for which the side of the terminator statistics is not good enough. Moreover, that explains also why the mean profile usually extends to a broader altitude range than the profiles by latitude bin or side of the terminator.

The mean values are computed on the logarithm of the upper limit densities and VMRs weighted by the uncertainties. The uncertainties on the mean profiles are computed as the average of the uncertainties of the individual profiles. The 1-σ variability are the weighted standard deviations of the logarithm of the upper limit densities and VMRs. As a consequence, the coloured envelopes in the following depict the variabilities, while the mean uncertainties are displayed by the dashed lines.

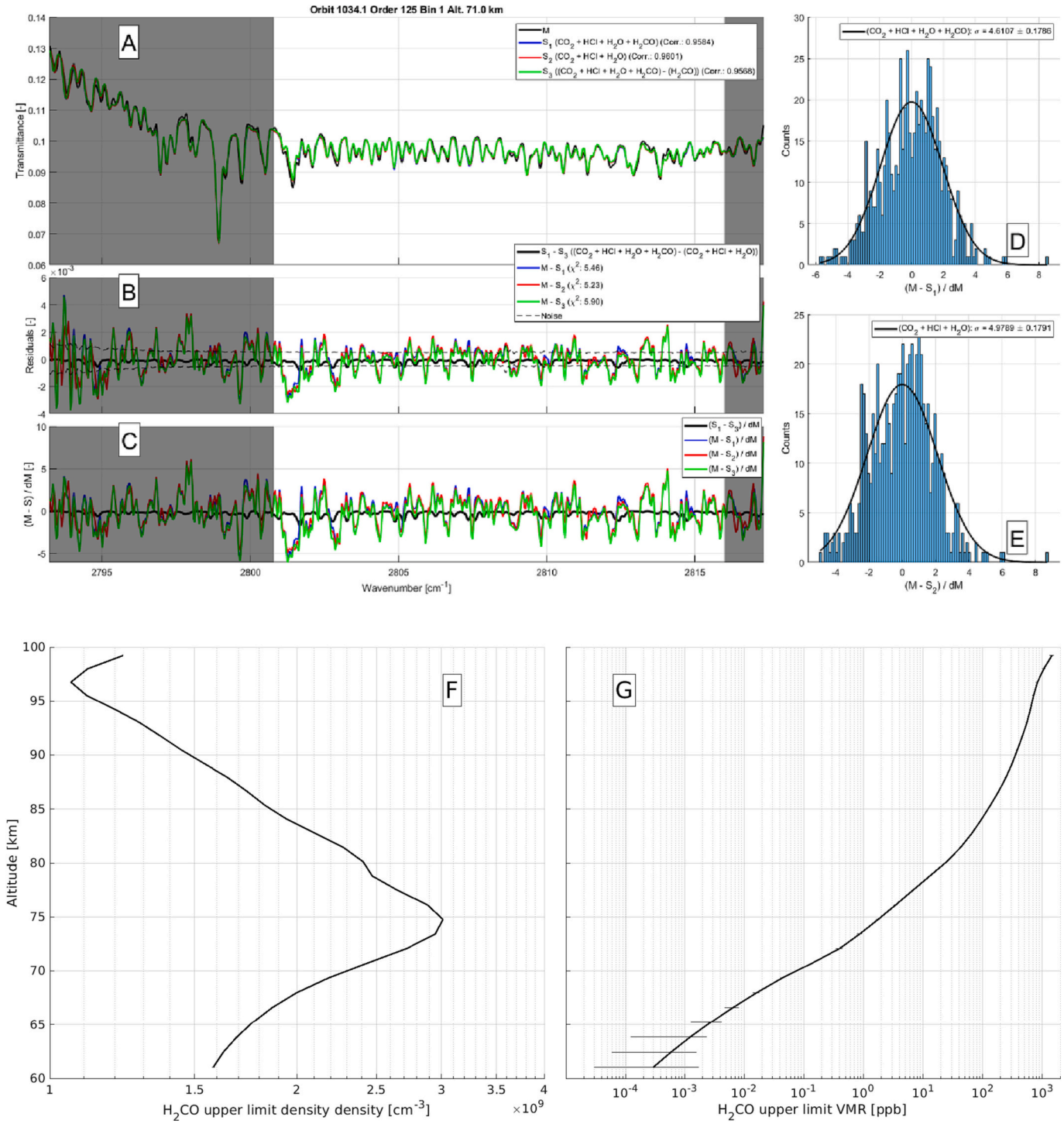

Fig. 2. Example of non-detection of H_2CO during occultation 1034.1 measured in order 125 and bin #1 at an altitude of 69.7 km. Panel A depicts the measured spectrum (M in black), the synthetic spectrum considering the major and minor species CO_2, HCl, H_2O, and H_2CO (S_1 in blue), the synthetic spectrum considering the major species CO_2, HCl, and H_2O only (S_2 in red), and the synthetic spectrum considering the major and minor species CO_2, HCl, H_2O, and H_2CO from which the signature of the targeted minor species H_2CO is set to zero (S_3, in green). The values of the correlation coefficients between the measured and synthetic spectra are given in the legend. The black-shaded wavenumber regions correspond to the regions that are not used to check the criteria defined in Section 5. Panel B shows the noise of the measurement (dashed black lines, dM), H_2CO contribution to the synthetic spectrum in black (S_1–S_3), residuals between the measured and synthetic spectra with major and minor species in blue (M–S_1), residuals between the measured and synthetic spectra considering the major species only in red (M–S_2), and residuals between the measured and synthetic spectrum considering the major and minor species CO_2, HCl, and H_2O from which the signature of the targeted minor species H_2CO is set to zero (M–S_3). The values of χ^2_ν are given in the legend. In Panel C are the residuals weighted by the noise, which is used to compute the χ^2_ν. Panel D is the histogram of the distribution of the residuals weighted by the uncertainties of the major and minor species fit (M–S_1) and fit of the distribution by a Gaussian. Panel E is the histogram of the distribution of the residuals weighted by the uncertainties of the major species and the non-targeted minor species fit (M–S_2) and fit of the distribution by a Gaussian. Panel F is the H_2CO upper limit number density profile for the whole occultation as a function of the altitude, while Panel G is the corresponding H_2CO upper limit VMR profile, computed from the simultaneously observed CO_2 vertical profile and the CO_2 VMR from VIRA. In these two panels, the horizontal bars are the uncertainties. (For interpretation of the references to colour in this figure legend, the reader is referred to the web version of this article.)

Table 3
Number of observations of each species as a function of the absolute latitude and side of the terminator.

Species	0°–30°	30°–60°	60°–80°	80°–90°	AM	PM	Total
H_2CO	16	17	35	24	59	33	92
O_3	6	8	12	10	22	14	36
NH_3	34	30	38	30	63	69	132
HCN	91	82	110	118	209	192	401
N_2O	1	2	10	10	15	8	23
NO_2	25	29	31	41	62	64	126
NO	53	62	75	80	143	127	270
HO_2	16	17	18	14	30	35	65

In each occultation, the spectra for which the baseline could not be determined with uncertainties lower than 100% are discarded in the following. This happens at low altitude (usually below ~75 km) when the signal is low and the absorption by the main gases (CO_2, CO, H_2O/HDO, HCl, and HF) is large, meaning that their absorption lines are optically thick, which prevents from precisely determining the value of the baseline corresponding to the absorption by the atmospheric aerosols. This explains why the mean upper limit number density and VMR profiles usually do not expand lower than 70–75 km.

The VMRs are computed considering the total number density combining the SOIR simultaneously derived CO_2 number densities and considering the CO_2 VMR from VIRA. Consequently, in the figures presented in the next sections, there is no direct multiplication factor between the number density profiles and the corresponding VMR profiles.

7.2. Formaldehyde

H_2CO was targeted 92 times during the VEx era. No reports of H_2CO measurements were found in the literature, even though papers from the last century discussed the possibility of finding formaldehyde in the Venus atmosphere (Wildt, 1940; Otroshchenko and Surkov, 1974).

We present in Fig. 3A the mean upper limit number density profiles from the measurements, separated by the side of the terminator and considering the full database, and in Fig. 3B, the corresponding mean upper limit VMR; the coloured envelopes correspond to the 1-σ variability and the dashed lines to the mean uncertainties. Fig. 3C and D provide the same quantities for bins of absolute latitude. The mean upper limit number densities are nearly constant with altitude, varying between $2.1 \times 10^9 \pm 10^7$ cm^{-3} at 65 km and $2.3 \times 10^9 \pm 3.4 \times 10^5$ cm^{-3} at 98 km. The mean value at 80 km equals $2.8 \times 10^9 \pm 3 \times 10^6$ cm^{-3} with a variability equal to a factor of 0.36. The corresponding VMRs have a positive slope, varying between 10.1 ± 0.5 ppt (parts-per-trillion, 10^{-12}) at 65 km and 14.8 ± 4.3 ppm at 98 km. The mean VMR value at 80 km equals to 43 ± 6 ppb with a variability factor equal to 0.23.

We see that the morning number upper limit density profiles are smaller than the evening ones; however, both profiles always remain within the variability envelope of the other one. In terms of VMR, the morning and evening profiles are very similar over the whole altitude range.

Fig. 2D shows that the highest latitude (80°-90°) H_2CO VMR upper limit is always smaller than for other latitude bins, while the lowest latitude (0°-30°) is always larger than the other ones.

A recent photochemical model study conducted by Spacek et al. (2023) suggested that formaldehyde could potentially be present at a level of 64 ppt at 60 km altitude. The SOIR upper limit obtained 5 km higher in altitude is ~6 times smaller than this simulated value by Spacek et al. (2023). Therefore, although both results could potentially agree, the SOIR upper limit provides a significant constraint on the hypothesis proposed in their study.

7.3. Ozone

Thirty-seven occultations targeted orders in which ozone has absorption lines. Fig. 4A presents the mean number density upper limit profile obtained from the observations, with the envelope depicting the 1-σ variability and the dashed lines the mean uncertainties. Only upper limit profiles for the whole database, the morning and evening sides of

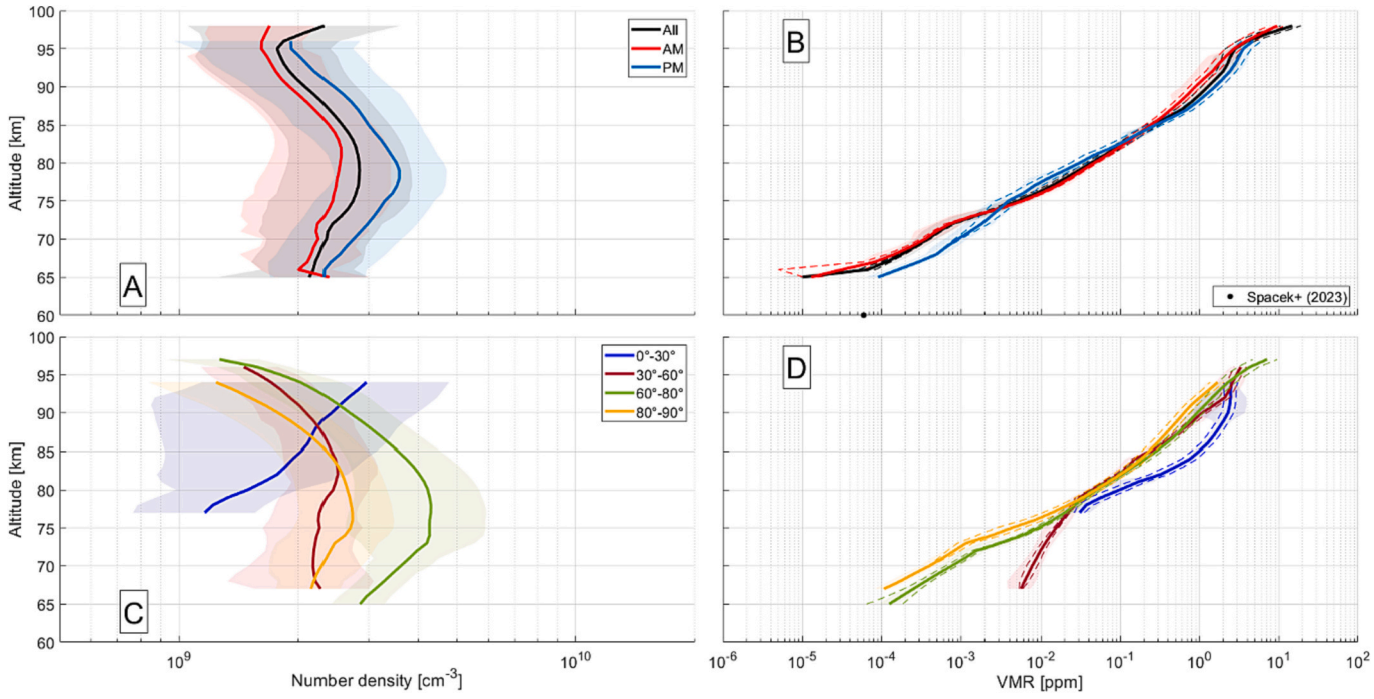

Fig. 3. H_2CO upper limit number densities (Panels A and C) and VMRs (Panels B and D) considering the total number density from the SOIR simultaneously measured CO_2 profiles. Panels A and B show the mean profiles for the whole database and by side of the terminator; Panels C and D show the mean profiles by latitude bins, assuming hemispherical symmetry. The dashed lines show the mean uncertainty, while the envelopes represent the 1-σ variability. In Panel B, the black marker corresponds to the results of the chemical model of Spacek et al. (2023).

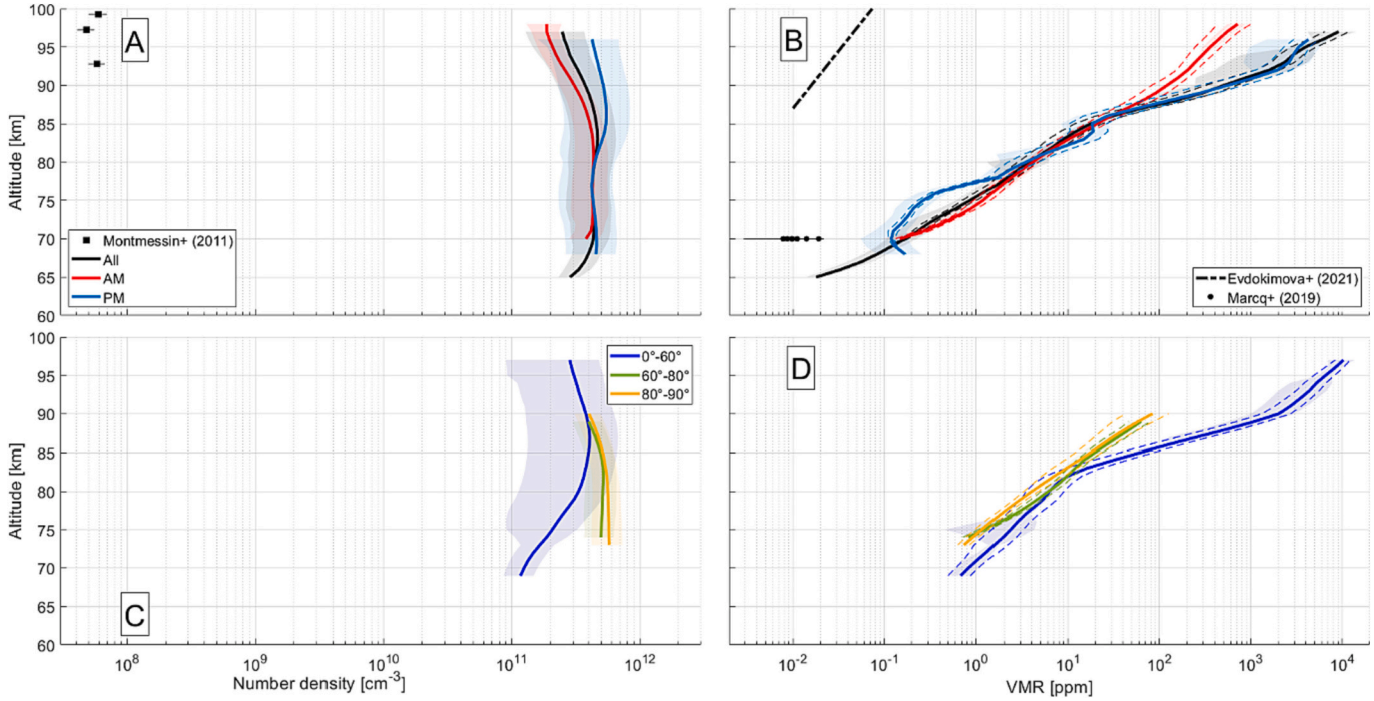

Fig. 4. O_3 upper limit number densities (Panels A and C) and VMRs (Panels B and D) considering the total number density from the SOIR simultaneously measured CO_2 profiles. Panels A and B show the mean profiles for the whole database and by side of the terminator; Panels C and D show the mean profiles by latitude bins (bins 0°-30° and 30°-60° were joined to have enough statistics), assuming hemispherical symmetry. The dashed lines show the mean uncertainty, while the envelopes represent the 1-σ variability. In Panel A, the squared markers are the detections by Montmessin et al. (2011), and in Panel B the black dash-dotted line is the mean profile from Evdokimova et al. (2021), and the black dots the mean latitudinal values from Marcq et al. (2019).

the terminator, and the 0–60°, 60°-80°, and 80°-90° absolute latitude bins are provided because the statistics are not robust enough to provide values for the 0°-30° and 30°-60° latitude bin regions separately. The mean profile shows a nearly constant with altitude, varying between 2.8 $\times$ 10^{11} $\pm$ 2 $\times$ 10^{9} cm^{-3} at 65 km and 2.4 $\times$ 10^{11} $\pm$ 10^{8} cm^{-3} at 97 km; the mean value at 80 km is equal to 4.44 $\times$ 10^{11} $\pm$ 1.1 $\times$ 10^{9} cm^{-3}, with a variability factor equal to 0.38. Fig. 4B shows the corresponding mean VMR profiles, which all exponentially increase with altitude, since the number density profile is nearly constant, with a mean value varying between 18 $\pm$ 0.12 ppb at 65 km and 9131 $\pm$ 2685 ppm at 97 km; the mean value at 80 km is equal to 3.76 $\pm$ 5.7 ppm with a variability factor of 0.65. There is no sign of side of the terminator dependence of the ozone upper limit VMR profile. At the highest latitudes, the O_3 VMR upper limit does not exceed 84.2 $\pm$ 41.5 ppm at 90 km, is of the same order of magnitude as the sub-polar latitude bin and remains below the nominal value defined for the low- to mid-latitude region.

Ozone was detected for the first time during a few occultations in the Venus mesosphere in the ultraviolet by the SPICAV/UV spectrometer on board Venus Express in stellar occultation mode (Montmessin et al., 2011), and the complete SPICAV/UV dataset was reanalysed later by Evdokimova et al. (2021). They both report on the presence of a non-permanent layer in the 90–120 km region, since ozone could not be detected during every observation. Later, Marcq et al. (2019) detected ozone in the SPICAV/UV nadir radiance spectra on the dayside at an altitude of 70 km with values between 4 and 20 ppb, and reports on a permanent layer with a latitudinal dependence with nearly all detections at latitudes larger than 45° coupled with an increase of the concentration while going from mid-latitudes towards the poles.

The Montmessin et al. (2011) number densities are plotted in Fig. 4A, and are more than three orders of magnitude smaller than the SOIR mean upper limit number densities, thus in agreement with the present work upper limits of detections.

The mean values of Evdokimova et al. (2021) are plotted in Fig. 4B. We see that the Evdokimova et al. (2021) values are one to three to five orders of magnitude smaller than the SOIR values, thus in agreement with the no-detections of the SOIR instrument. The upper limit values presented here cover a deeper altitude range and provide boundaries at altitudes lower than 87 km. Finally, the Evdokimova et al. (2021) values were reported on the nightside, while the profiles presented here were taken at the terminator.

Agreement with Marcq et al. (2019) is good, since the mean SOIR upper-limit VMR at 72 km are one order of magnitude larger than their reported values at 70 km. Their values were taken on the dayside, while the values reported here are at the terminator. Fig. 7 of that paper seems to indicate a decrease of the mean detected ozone close to the terminator (in the 6–7 h and 17–18 h LST bins), with values close to 4 ppm. The latitude dependence of ozone found by Marcq et al. (2019) cannot be assessed considering the SOIR upper limit dataset because of the insufficient statistical latitude coverage.

The SOIR derived mid-latitude upper limit VMRs are larger than the high-latitude ones by nearly an order of magnitude above 85 km. These results are expected if O_3 density follows the available abundance of O_2, which is known to experience strong downward transport over the Venus poles. Ozone in the Venus mesosphere is related to the nightside recombination of dayside atomic oxygen produced by CO_2 photolysis, which is transported by the upper-atmosphere subsolar to antisolar circulation (Montmessin et al., 2011).

7.4. Ammonia

Four hundred thirty occultations measured orders in which ammonia has absorption bands.

Fig. 5A shows the mean upper limit density profiles for the whole database, morning, and evening occultations, their associated mean uncertainties, and 1-σ variabilities. The mean number density values vary between 1.9 $\times$ 10^{10} $\pm$ 3 $\times$ 10^{8} cm^{-3} at 98 km and 9.2 $\times$ 10^{10} $\pm$ 1.2 $\times$ 10^{9} cm^{-3} at 65 km; the mean value at 80 km is equal to 8.7 $\times$ 10^{10} $\pm$ 6.5 $\times$ 10^{8} cm^{-3} with a variability factor of 0.55. The mean morning and

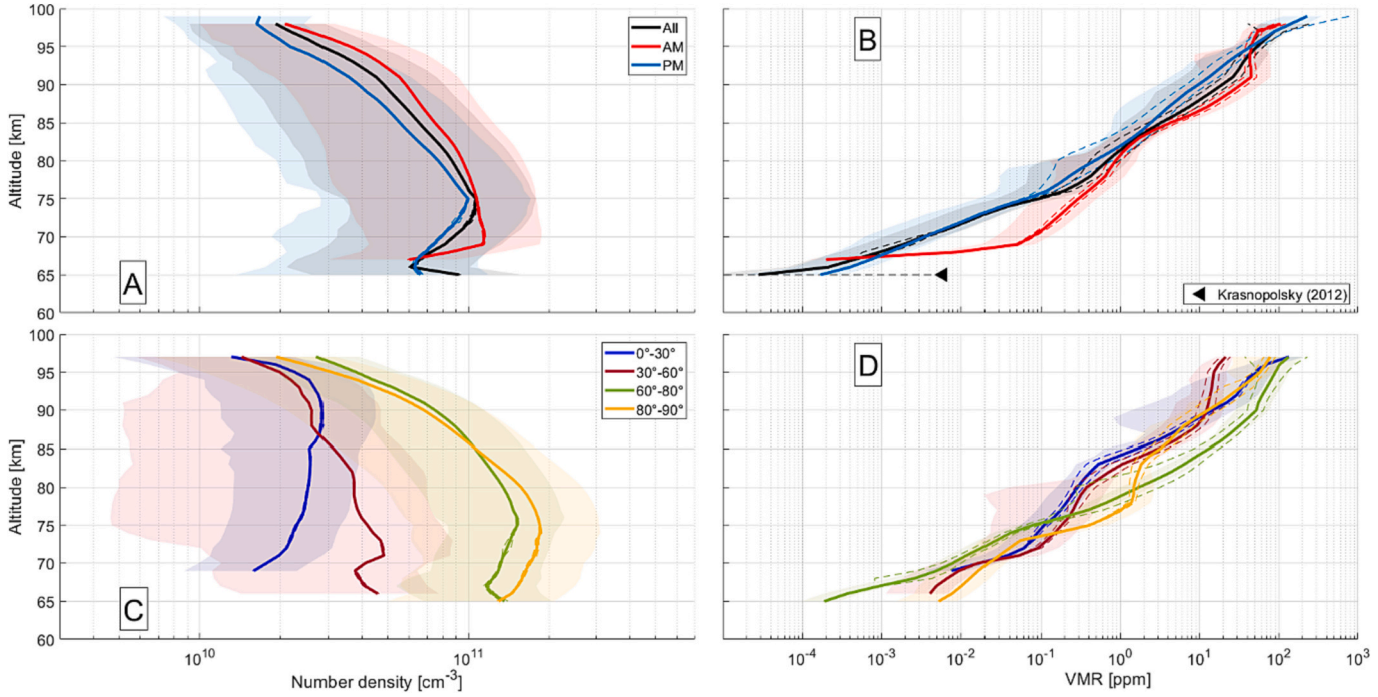

Fig. 5. NH_3 upper limit number densities (Panels A and C) and VMRs (Panels B and D) considering the total number density from the SOIR simultaneously measured CO_2 profiles. Panels A and B show the mean profiles for the whole database and by side of the terminator; Panels C and D show the mean profiles by latitude bins, assuming hemispherical symmetry. The dashed lines show the mean uncertainty, while the envelopes represent the 1-σ variability. The triangle in Panel B is the Krasnopolsky (2012) upper limit of detection.

evening profiles and the mean profile for the whole database all lie within the variability of the other ones.

Fig. 5B shows the respective VMR profiles and associated uncertainties and 1-σ variabilities. The mean VMR values vary from 28.4 ± 0.6 ppt at 65 km to 142.3 ± 103 ppm at 98 km; the mean VMR at 80 km is equal to 0.69 ± 0.28 ppm with a variability factor of 0.86. Fig. 5C shows the latitude bin mean profiles, and Fig. 5D their equivalent in VMR. No trend relative to the morning or evening side of the terminator is observed regarding VMR.

Only an NH_3 upper limit above the cloud has been found in the

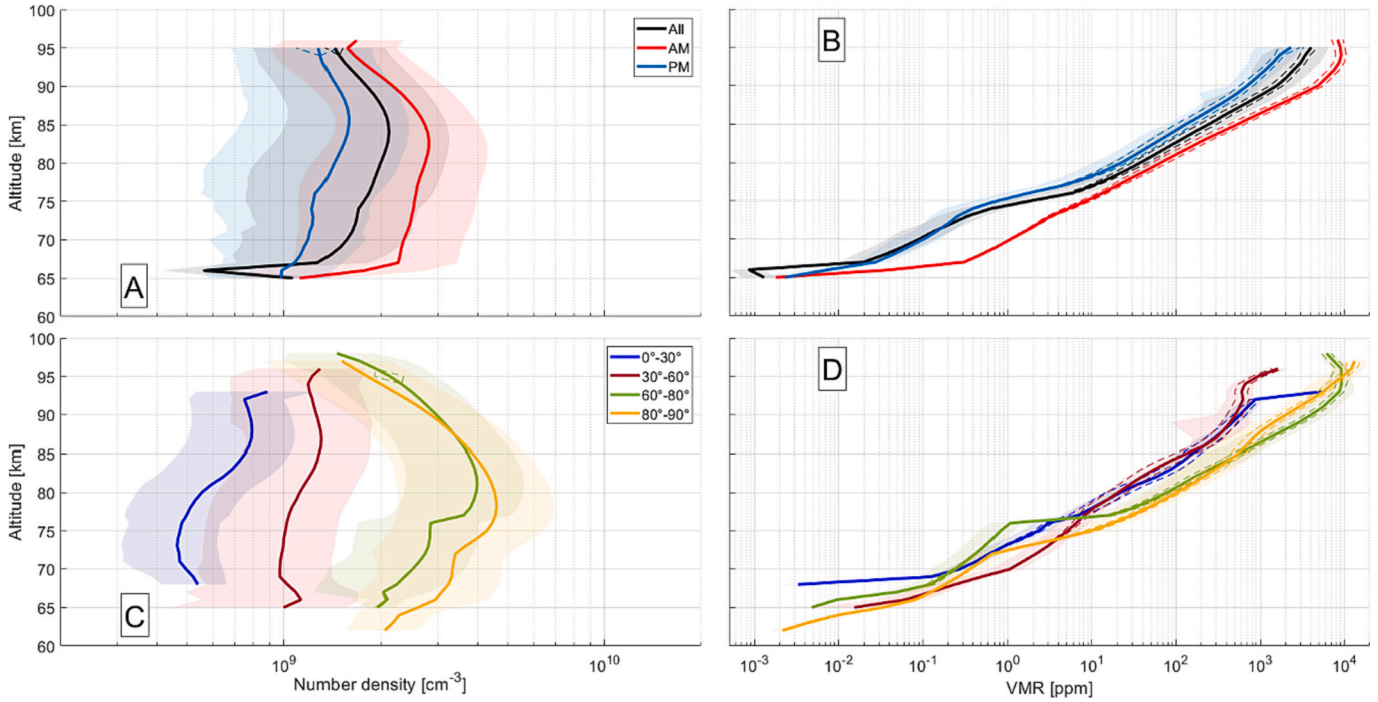

Fig. 6. HCN upper limit number densities (Panels A and C) and VMRs (Panels B and D) considering the total number density from the SOIR simultaneously measured CO_2 profiles. Panels A and B show the mean profiles for the whole database and by side of the terminator; Panels C and D show the mean profiles by latitude bins, assuming hemispherical symmetry. The dashed lines show the mean uncertainty, while the envelopes represent the 1-σ variability.

literature (Krasnopolsky, 2012), measured from the IRTF-NASA ground-based facilities using the CSHELL spectrograph in the infrared. The upper limit value reported in this work is a factor ~ 200 larger than the mean value reported in this work. SOIR has a resolution of ~21,000, while CSHELL reports a resolution of 20,000 to 30,000, thus similar to SOIR. NH_3 was detected in the Venus lower-cloud layer by the Venera 8 probe (Surkov et al., 1973) and after reanalysis in the Pioneer Venus probe data (Mogul et al., 2021). The latest does not provide concentrations in their work.

7.5. Hydrogen cyanide

Four hundred and three occultations targeted HCN.

In Fig. 6A, we provide the mean HCN upper limit density values for the terminator's morning and evening sides and the whole database. The evening profile has lower upper limit values than the morning one by a factor of 2, except below 68 km. The mean values vary from $1.06 \times 10^9 \pm 10^7$ cm^{-3} at 65 km to $1.43 \times 10^9 \pm 9 \times 10^7$ cm^{-3} at 95 km; the mean upper limit number density value at 80 km is equal to $2 \times 10^9 \pm 6 \times 10^6$ cm^{-3}. The coloured regions correspond to the variability, equal to a factor of 0.59 at 80 km. Fig. 6B shows the corresponding upper limit VMRs. The values increase with altitude from 1.3 ± 0.01 ppb at 65 km to 4048 ± 806 ppm at 95 km; the mean value at 80 km is equal to 38.3 ± 7.9 ppm with a variability factor of 0.57. Fig. 6C and Fig. 6D are the mean upper limits for the different latitude bins in number density and VMR, respectively. Unlike other species, the HCN upper limit VMR and number densities appear to maximise at high latitudes and minimise at lower latitudes above 75 km; below, the sub equatorial bins shows maximum values.

The reanalysis of the Pioneer Venus Large Probe mass spectrometer data by Mogul et al. (2021) suggested the presence of hydrogen cyanide in the Venus clouds in the 64.1 to 51.3 km altitude region. The presence of reduced nitrogen-bearing species such as HCN in an oxidising atmosphere would indicate redox disequilibria in the clouds. In line with other teams' findings, Mogul et al. (2021) speculated on potential sources of such species, including volcanic emissions and biological activity. However, although they do not provide a quantitative estimate of HCN abundance in the clouds, the SOIR upper limit of 1.3 ppb at 65 km altitude probably does not support their findings. Instead, it imposes a strong constraint on the hypothetical mechanisms they proposed.

7.6. Nitrous oxide

Orders in which N_2O absorbs were only targeted 23 times during the whole VEx mission.

N_2O was shown to be a product of electric discharges in atmospheres like the early Earth, Venus, and Mars (Krasnopolsky and Parshev, 1983; Nna Mvondo et al., 2001). However, it could not be detected by the SOIR instrument above the cloud layer. Mogul et al. (2021) claimed its detection in their reanalysis of the Pioneer Venus Large Probe mass spectrometer in the 64.1 to 51.3 km altitude range but did not provide concentrations.

Fig. 6A shows the mean upper limit density profile computed from all the SOIR observations. The mean values vary from $7 \times 10^9 \pm 2 \times 10^7$ cm^{-3} at 66 km to $5.95 \times 10^9 \pm 2 \times 10^7$ cm^{-3} at 96 km; the mean value at 80 km is equal to $1.7 \times 10^{10} \pm 3 \times 10^8$ cm^{-3}. At 80 km, the mean variability corresponds to a factor of 0.53. In Fig. 7B, the mean upper limit VMRs vary between 0.52 ± 0.04 ppb at 66 km and 22.5 ± 7.1 ppm at 96 km; the mean value at 80 km is equal to 0.14 ± 0.02 ppm with a variability factor of 0.2. In both panels, the grey envelope is the variability, and the dashed lines are the mean uncertainties. Because of the poor statistics, see Table 3, we do not show the morning and evening mean profiles.

Fig. 7C and Fig. 7D show the mean upper limit values for the 60°-80° and 80°-90° bins, for which the statistics are large enough to compute the mean profiles. No latitude dependence is observed.

7.7. Nitrogen dioxide

One hundred twenty-six occultations targeted orders in which NO_2 has absorption.

No NO_2 detection above the cloud layer could be found in the

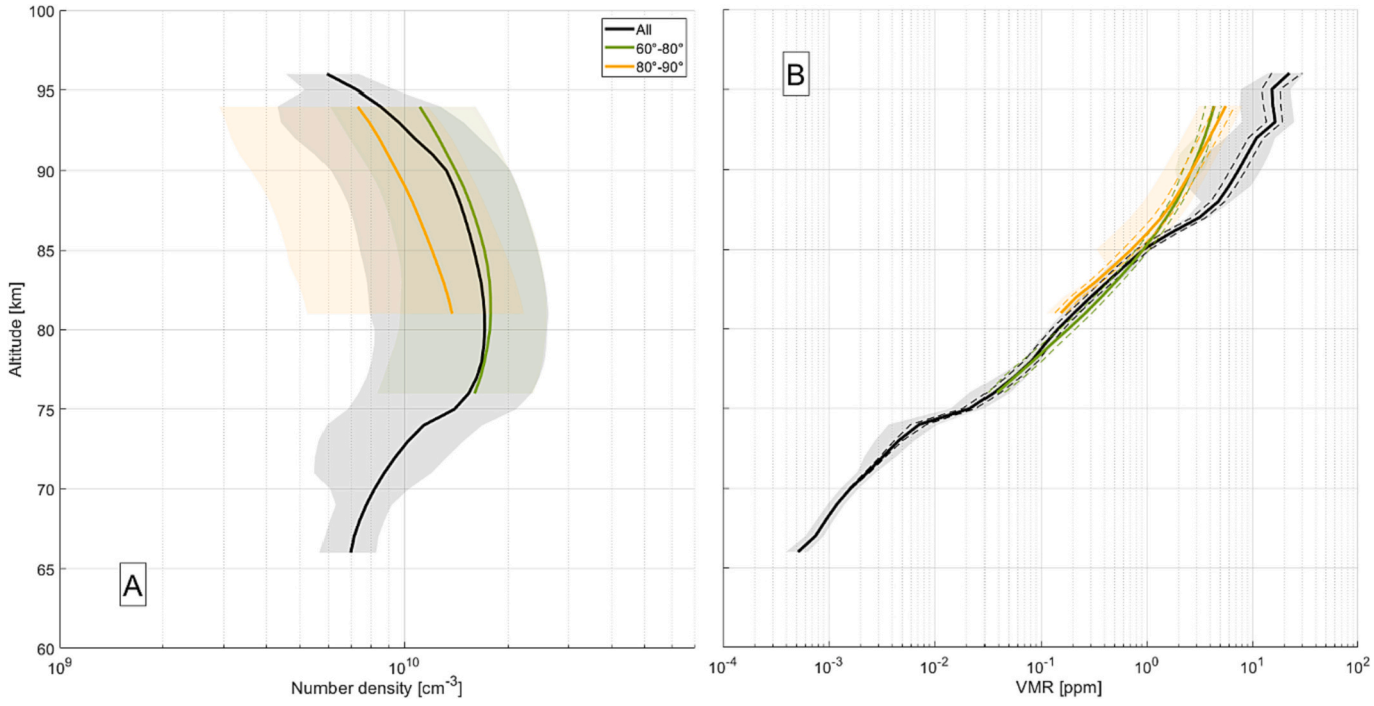

Fig. 7. N_2O upper limit number densities (Panel A) and VMRs (Panel B) considering the total number density from the SOIR simultaneously measured CO_2 profiles for the whole database and the 60°-80° and 80°-90° absolute latitude bins. The dashed lines show the mean uncertainty, while the envelopes represent the 1-σ variability.

literature. However, as for N_2O, models predict its presence if lightning occurs within the clouds of Venus (Krasnopolsky and Parshev, 1983; Nna Mvondo et al., 2001).

Fig. 7A shows the morning, evening, and whole database mean upper limit density profiles, with the coloured envelopes depicting the variability and the dashed lines the mean uncertainties. The profiles decrease with altitude, from $1.3 \times 10^{10} \pm 2 \times 10^{7}$ cm^{-3} at 65 km to $4.7 \times 10^{9} \pm 10^{6}$ cm^{-3} at 98 km; the mean value at 80 km is equal to $9.8 \times 10^{9} \pm 10^{6}$ cm^{-3}. The variability factor at 80 km is equal to 0.43. There are no significant differences in terms of variability between the morning and evening profiles. Fig. 8B displays the upper limit VMRs, varying from 172 ± 4 ppt at 65 km to 229 ± 547 ppm at 98 km; the mean value at 80 km is equal to 0.47 ± 0.32 ppm with a variability factor of 0.72. Fig. 8C and D show the mean profiles for the different latitude bins for the number density and VMR, respectively. No latitude dependence is observed in terms of VMR.

7.8. Nitrogen monoxide

Two-hundred seventy-one occultations scanned orders in which NO has absorption lines.

Fig. 9A shows the upper limit number density profiles for the morning, evening, and whole database, which vary from $3.4 \times 10^{11} \pm 1.9 \times 10^{9}$ cm^{-3} at 64 km and $1.9 \times 10^{11} \pm 10^{9}$ cm^{-3} at 95 km, with a mean upper limit number density at 80 km of $3.18 \times 10^{11} \pm 10^{9}$ cm^{-3}. The evening profile is 2 to 3 times smaller than the morning one, and the variability factor at 80 km equals 0.41. Fig. 9B shows the corresponding VMRs, which vary from 0.56 ± 0.03 ppb at 64 km and 643 ± 116 ppm at 95 km; the mean value at 80 km is equal to 6.15 ± 1.84 ppm with a variability factor of 0.4.

Fig. 9C (number density) and Fig. 9D (VMR) are the mean absolute latitude upper limit profiles. No latitude dependence is observed.

Krasnopolsky (2006) detected NO in the cloud layer and estimated a value of 5.5 ± 1.5 ppb at 60 km using a radiative model. The NO value above the cloud top found in this work is smaller by an order of magnitude.

7.9. Hydroperoxyl

Sixty-five solar occultations targeted orders in which HO_2 has absorptions lines. No detection of hydroperoxyl in the Venus atmosphere has been reported to date.

In Fig. 10A, we provide the mean upper limit number density profiles for HO_2 detection for the morning, evening, and the whole database, which vary from $1.2 \times 10^{10} \pm 4 \times 10^{9}$ cm^{-3} at 65 km to $8.2 \times 10^{9} \pm 2 \times 10^{7}$ cm^{-3} at 98 km; the mean value at 80 km is equal to $1.12 \times 10^{10} \pm 10^{9}$ cm^{-3}, with a variability factor of 0.3.

Fig. 10B provides the upper limit VMR profiles, which vary from 40 ± 1 ppt at 65 km to 28.6 ± 6.6 ppm at 98 km; the mean value at 80 km is equal to 99.5 ± 62.2 ppb, with a variability factor of 0.35.

Fig. 10C shows the mean absolute latitude bin upper limit number density, and Fig. 10D is the equivalent VMR. The 30°-60° bin shows a larger upper limit density than the other bins. In terms of VMR, there is no evidence of a latitudinal trend.

8. Conclusion

In this work, we analyse the SOIR/Venus Express spectra in search of oxygen-, nitrogen-, and carbon-bearing species with spectral signatures of the order of magnitude of the SOIR noise level. First, we use the same technique as in Mahieux et al. (2023a) to detect SO_2, SO_3, OCS, CS, and CS_2 in the Venus atmosphere. The method did not return positive detections of the gases targeted in this work: H_2CO, O_3, HCN, NH_3, N_2O, NO_2, NO, and HO_2. Instead, we provide mean upper limit number density and volume mixing ratio profiles of the gases, computed using the approach presented in Trompet et al. (2021), and their associated uncertainties and 1-σ variabilities. The majority of these species show no sensitivity to the latitude of observation except for O_3, which displays lower upper limit values in the high polar regions (presumably due to polar O_2 downwelling), and HCN, which shows the opposite latitudinal trend.

For H_2CO, we obtain mean upper limit VMR at 80 km 43 ± 6 ppb ($2.8 \times 10^{9} \pm 3 \times 10^{6}$ cm^{-3}), and 10.1 ± 0.5 ppt at 65 km, which is more

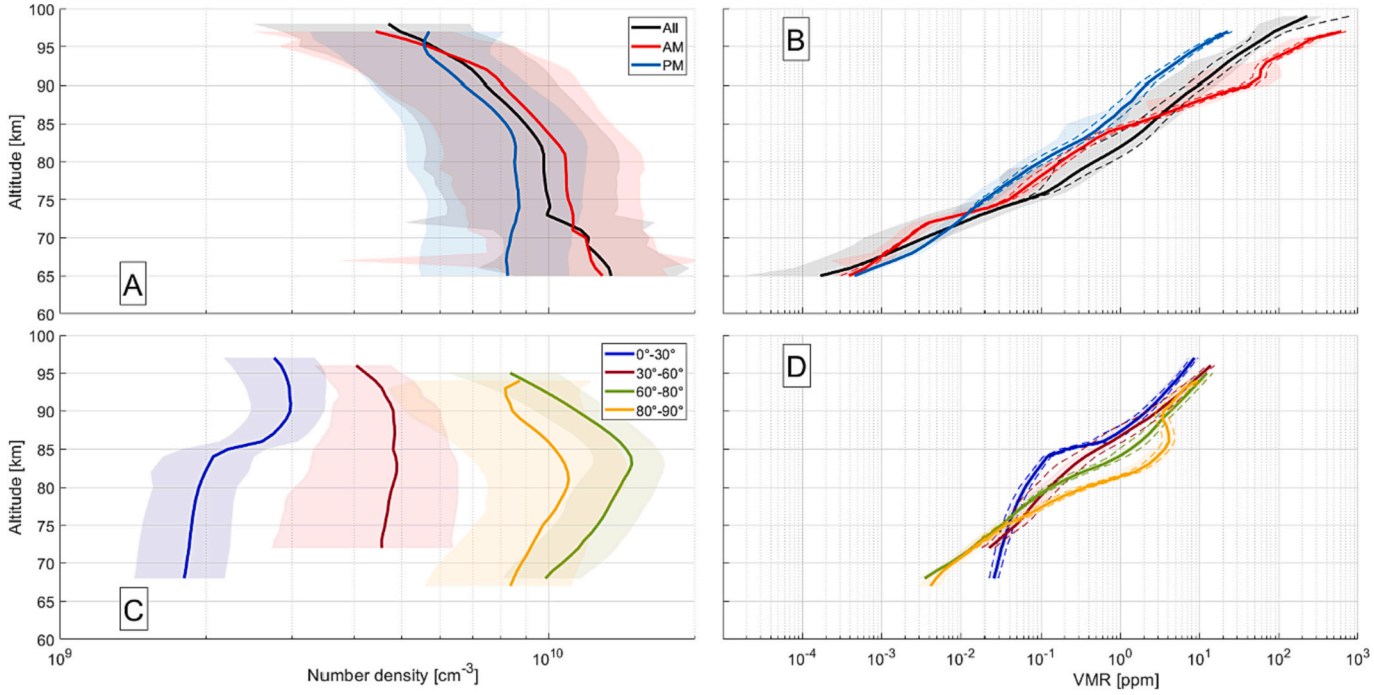

Fig. 8. NO_2 upper limit number densities (Panels A and C) and VMRs (Panels B and D) considering the total number density from the SOIR simultaneously measured CO_2 profiles. Panels A and B show the mean profiles for the whole database and by side of the terminator; Panels C and D show the mean profiles by latitude bins, assuming hemispherical symmetry. The dashed lines show the mean uncertainty, while the envelopes represent the 1-σ variability.

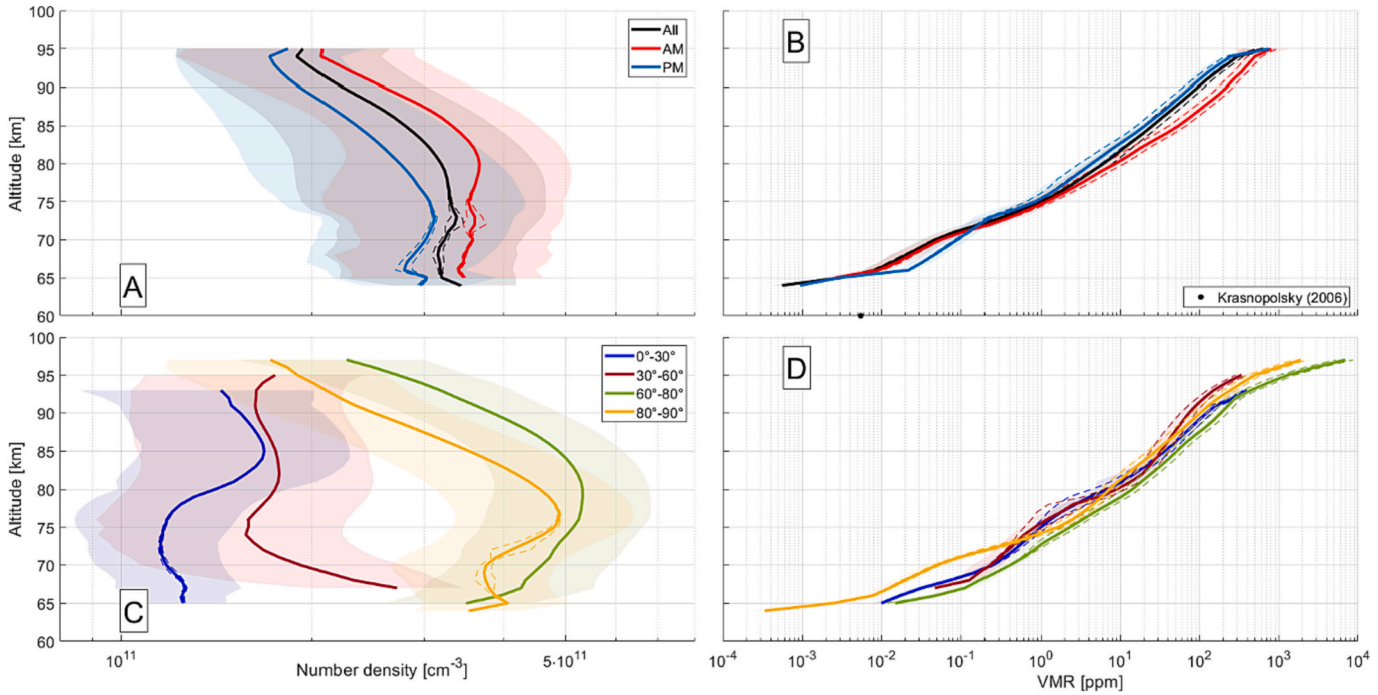

Fig. 9. NO upper limit number densities (Panels A and C) and VMRs (Panels B and D) considering the total number density from the SOIR simultaneously measured CO_2 profiles. Panels A and B show the mean profiles for the whole database and by side of the terminator; Panels C and D show the mean profiles by latitude bins, assuming hemispherical symmetry. The dashed lines show the mean uncertainty, while the envelopes represent the 1-σ variability. The black dot in Panel B is the extrapolated value from Krasnopolsky (2006).

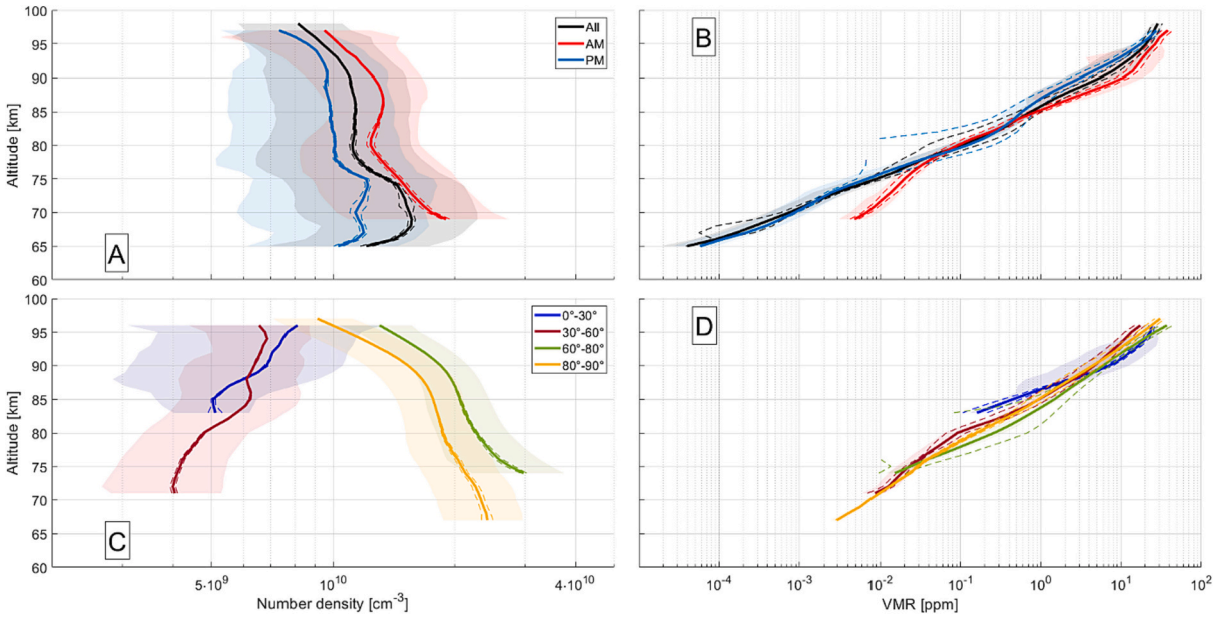

Fig. 10. HO_2 upper limit number densities (Panels A and C) and VMRs (Panels B and D) considering the total number density from the SOIR simultaneously measured CO_2 profiles. Panels A and B show the mean profiles for the whole database and by side of the terminator; Panels C and D show the mean profiles by latitude bins, assuming hemispherical symmetry. The dashed lines show the mean uncertainty, while the envelopes represent the 1-σ variability.

than ~6 times smaller than the value predicted by the photochemical model of Spacek et al. (2023) 5 km lower.

For O_3, we report an upper limit value of 3.76 ± 5.7 ppm at 80 km ($4.44 \times 10^{11} \pm 1.1 \times 10^{9}$ cm^{-3}). The mean upper limit concentrations above 87 km are at least three times larger than the mean measured ozone values reported by Evdokimova et al. (2021) on the Venus nightside, thus in agreement with that dataset since such low values could not have been detected by SOIR. The upper limit number densities are also in agreement with the Montmessin et al. (2011) number densities, since the SOIR upper limit number densities are three orders of magnitude larger. Comparison with Marcq et al. (2019), which reported detection of ozone on the dayside above the cloud top, also shows good agreement since their values are at least ten times smaller than the SOIR upper limit values. However, because of the few SOIR ozone observations, no latitude trend could be observed in our dataset, and thus does not allow to comment on the latitude dependence reported by that work.

For NH_3, the mean upper limit VMR at 80 km is equal to 0.69 ± 0.28 ppm ($8.7 \times 10^{10} \pm 6.5 \times 10^8$ cm^{-3}) and 28.4 ± 0.6 ppt at 65 km, which is ~200 times smaller than the value computed by Krasnopolsky (2012) from detection in the lower cloud layer and using a radiative transfer model to infer it above the cloud top.

For HCN, the upper limit at 80 km equals a VMR of 38.3 ± 7.9 ppm ($2 \times 10^9 \pm 6 \times 10^6$ cm^{-3}).

We report a mean upper limit N_2O VMR at 80 km of 0.14 ± 0.02 ppm ($1.7 \times 10^{10} \pm 3 \times 10^8$ cm^{-3}). For NO_2, the mean upper limit at 80 km is equal to 0.47 ± 0.32 ppm ($9.8 \times 10^9 \pm 10^6$ cm^{-3}). The mean upper limit of NO at 80 km is equivalent to 6.15 ± 1.84 ppm ($3.18 \times 10^{11} \pm 10^9$ cm^{-3}), ten times smaller than the Krasnopolsky (2006) reported values above the cloud top.

Finally, for HO_2, the mean upper limit VMR at 80 km is equal to 99.5 ± 62.2 ppb ($1.12 \times 10^{10} \pm 10^9$ cm^{-3}).

Recent studies reported tentative detections of phosphine (Greaves et al., 2021; Greaves et al., 2023) and ammonia (Mogul et al., 2021) in the cloud layer. These findings have been interpreted as potential indications of biological activity in the clouds. While these PH_3 observations have been repeatedly questioned (e.g., Encrenaz et al. (2020); Trompet et al. (2021); Villanueva et al. (2021)), we here provide a strong constraint on previous NH_3 detections by reporting a stringent upper limit of 28.4 ± 0.6 ppt at 65 km altitude.

Declaration of Competing Interest

The authors declare that they have no known competing financial interests or personal relationships that could have appeared to influence the work reported in this paper.

Data availability

The data are available on the ESA PSA repository and on the VESPA platform, as described in the text.

Acknowledgements

Venus Express is a planetary mission from the European Space Agency (ESA). We thank all ESA members who participated in the mission, particularly H. Svedhem and D. Titov. We thank our collaborators at IASB-BIRA (Belgium), Latmos (France), and IKI (Russia). The research program was supported by the Belgian Federal Science Policy Office and the European Space Agency (ESA, PRODEX program, contracts C 90268, 90113, 17645, 90323, and 4000107727). A. Mahieux was supported by the Marie Skłodowska-Curie Action from the European Commission under grant number 838587. S. Viscardy was supported by the Belgian Science Policy Office through the BrainBe MICROBE Project.

The mean upper limit profiles presented in the next sections will be made available on the VESPA platform https://vespa-client-dev.obspm.fr/planetary/data/ (Trompet et al., 2018).

Appendix A. List of the vibrational bands considered in each diffraction order

We provide the list of vibrational bands fitted in each order in Table 4.

Table 4
List of the vibrational bands by isotopologue used for the fits of the minor species (H_2CO, O_3, NH_3, HCN, N_2O, NO_2, NO, and HO_2). The notation follows the HITRAN standards (Gordon et al., 2017), except for NH_3 and NO, for which all the transitions are not listed because they are too numerous.

Order	Isotopologue	Vibrational band
113	$^{16}O^{12}C^{18}O$	20,003–00001, 20,002–00001
	$^{16}O^{12}C^{17}O$	20,003–00001
	$^{16}O^{13}C^{18}O$	20,002–00001
	$^{12}C^{32}S$	2–0
	$^{14}N_2^{16}O$	2000–0000
	$^{12}C^{16}O_2$	12,211–12,202
114	$^{16}O^{12}C^{18}O$	12,202–00001, 20,002–00001, 20,003–00001, 21,102–01101, 21,103–01101, 22,202–02201, 23,302–03301, 30,002–10,001, 30,003–10,001, 30,003–10,002, 30,004–10,002, 31,102–11,101, 31,103–11,102
	$^{16}O^{12}C^{17}O$	20,002–00001, 20,003–00001, 21,102–01101, 21,103–01101, 30,003–10,001, 30,003–10,002, 30,004–10,002
	$^{16}O^{13}C^{18}O$	20,002–00001, 20,003–00001, 21,102–01101, 30,002–10,001, 30,003–10,002
	$HD^{16}O$	020–000, 100–000
	$^{14}N_2^{16}O$	2000–0000
115	$^{16}O^{12}C^{18}O$	12,202–00001, 20,002–00001, 20,003–00001, 21,102–01101, 22,202–02201, 23,302–03301, 30,002–10,001, 30,003–10,001, 30,003–10,002, 31,102–11,101, 31,103–11,102
	$^{16}O^{12}C^{17}O$	20,002–00001, 20,003–00001, 21,102–01101, 21,103–01101, 22,202–02201, 30,002–10,001, 30,003–10,001, 30,003–10,002
	$^{16}O^{13}C^{18}O$	20,002–00001, 21,102–01101, 30,002–10,001, 30,003–10,002
	$HD^{16}O$	020–000, 100–000
	$^{14}N_2^{16}O$	2000–0000
123	$^{16}O^{12}C^{18}O$	20,001–00001, 21,101–01101, 30,002–10,002, 12,201–00001, 30,001–10,001
	$^{16}O^{12}C^{17}O$	20,001–00001, 21,101–01101
	$^{16}O^{13}C^{18}O$	20,001–00001, 21,101–01101
	$H^{35}Cl$	1–0
	$H^{37}Cl$	1–0
	$HD^{16}O$	100–000, 020–000
	$H_2^{12}C^{16}O$	100,000–000000
124	$^{16}O^{12}C^{18}O$	20,001–00001, 21,101–01101, 30,001–10,001, 22,201–02201, 30,002–10,002, 12,201–00001
	$^{16}O^{12}C^{17}O$	20,001–00001, 2110–101,101
	$^{16}O^{13}C^{18}O$	21,101–01101
	$H^{35}Cl$	1–0
	$H^{37}Cl$	1–0
	$HD^{16}O$	100–000, 020–000
	$^{32}S^{16}O_3$	002200E'-000000A1'
	$H_2^{12}C^{16}O$	100,000–000000, 000010–000000

(continued on next page)

Table 4 (*continued*)

Order	Isotopologue	Vibrational band
	$^{16}O^{12}C^{18}O$	20,001–00001, 21,101–01101, 30,001–10,001, 22,201–02201
	$^{16}O^{12}C^{17}O$	20,001–00001, 21,101–01101
	$H^{35}Cl$	1–0
125	$H^{37}Cl$	1–0
	$HD^{16}O$	100–000, 020–000
	$^{32}S^{16}O_3$	002200E'-000000A1'
	$H_2^{12}C^{16}O$	100,000–000000, 000010–000000
	$^{16}O^{12}C^{18}O$	20,001–00001, 21,101–01101, 30,001–10,001, 22,201–02201
	$^{16}O^{12}C^{17}O$	20,001–00001, 21,101–01101
	$H^{35}Cl$	1–0
126	$H^{37}Cl$	1–0
	$HD^{16}O$	100–000, 020–000
	$^{32}S^{16}O_3$	002200E'–000000A1'
	$^{12}C^{32}S_2$	2001–0000
	$H_2^{12}C^{16}O$	100,000–000000, 000010–000000
	$^{16}O^{12}C^{18}O$	21,101–01101, 30,001–10,001, 22,201–02201
	$^{16}O^{12}C^{17}O$	20,001–00001, 21,101–01101
	$H^{35}Cl$	1–0
127	$H^{37}Cl$	1–0
	$HD^{16}O$	100–000, 020–000
	$H_2^{12}C^{16}O$	100,000–000000, 000010–000000
	$^{16}O^{12}C^{18}O$	22,201–02201
	$^{16}O^{12}C^{17}O$	21,101–01101
	$H^{35}Cl$	1–0
128	$H^{37}Cl$	1–0
	$HD^{16}O$	100–000, 020–000
	$^{16}O^{12}C^{32}S$	1001–0000, 1111–0110
	$H_2^{12}C^{16}O$	100,000–000000
	$H^{35}Cl$	1–0
	$H^{37}Cl$	1–0
129	$HD^{16}O$	100–000, 020–000
	$^{16}O^{12}C^{32}S$	1001–0000, 1111–0110
	$^{14}N^{16}O_2$	101–000, 111–010
	$H^{35}Cl$	1–0
	$H^{37}Cl$	1–0
130	$HD^{16}O$	100–000, 020–000
	$^{16}O^{12}C^{32}S$	1001–0000, 1111–0110
	$^{14}N^{16}O_2$	101–000, 111–010
	$^{12}C^{16}O_2$	31,104–02201, 31,104–10,001
	$^{16}O^{12}C^{18}O$	01111–00001, 02211–01101, 10,011–01101, 30,004–01101
	$^{16}O^{12}C^{17}O$	01111–00001
	$H^{35}Cl$	1–0
134	$H^{37}Cl$	1–0
	$H_2^{16}O$	020–000
	$HD^{16}O$	100–000, 020–000
	$^{16}O_3$	003000
	$^{12}C^{16}O_2$	31,104–02201, 31,104–10,001
	$^{16}O^{12}C^{18}O$	10,011–01101, 30,004–01101
	$^{16}O^{12}C^{17}O$	01111–00001
	$H^{35}Cl$	1–0
135	$H^{37}Cl$	1–0
	$H_2^{16}O$	020–000
	$HD^{16}O$	020–000
	$^{16}O_3$	003000
	$^{12}C^{16}O_2$	13,302–00001, 14,402–01101, 21,102–00001, 21,103–00001, 21,112–00011, 22,202–01101, 22,203–01101, 22,213–12,201, 23,302–02201, 24,402–03301, 25,502–04401, 30,003–01101, 31,102–10,001, 31,103–02201, 31,103–10,001, 31,103–10,002, 32,202–11,101, 32,203–03301, 32,203–11,102, 33,303–12,202, 40,003–11,101, 40,004–11,102, 41,103–20,002, 41,104–12,202, 41,104–20,003
	$^{13}C^{16}O_2$	21,102–00001, 21,113–11,101, 22,202–01101, 23,302–02201, 24,402–03301, 30,003–01101, 31,102–10,001, 31,103–02201, 31,103–10,002, 32,203–11,102, 40,004–11,102
145	$^{16}O^{12}C^{18}O$	21,102–00001, 22,202–01101, 23,302–02201, 30,002–01101, 30,003–01101, 31,102–10,001, 31,103–10,002
	$^{16}O^{12}C^{17}O$	21,102–00001, 21,103–00001, 22,202–01101, 30,003–01101
	$^{16}O^{13}C^{18}O$	21,102–00001
	$H_2^{16}O$	001–000, 020–000, 100–000
	$H^{12}C^{14}N$	1000–0000
	$^{12}C^{16}O_2$	13,302–00001, 14,402–01101, 21,102–00001, 21,103–00001, 21,112–00011, 22,202–01101, 22,203–01101, 22,213–12,201, 23,302–02201, 24,402–03301, 25,502–04401, 30,002–01101, 30,003–01101, 31,102–10,001, 31,103–02201, 31,103–10,001, 31,103–10,002, 31,114–21,102, 32,202–11,101, 32,203–03301, 32,203–11,102, 33,302–12,201, 33,303–12,202, 40,003–11,101, 40,004–11,102, 41,103–20,002, 41,104–12,202, 41,104–20,003
	$^{13}C^{16}O_2$	20,013–10,001, 21,102–00001, 21,113–11,101, 22,202–01101, 23,302–02201, 24,402–03301, 30,002–01101, 30,003–01101, 31,102–10,001, 31,103–02201, 31,103–10,002, 32,203–11,102, 40,004–11,102
146	$^{16}O^{12}C^{18}O$	21,102–00001, 22,202–01101, 23,302–02201, 30,002–01101, 30,003–01101, 31,102–10,001, 31,103–10,002
	$^{16}O^{12}C^{17}O$	21,102–00001, 22,202–01101, 30,002–01101, 30,003–01101
	$^{16}O^{13}C^{18}O$	20,013–10,001, 21,102–00001
	$H_2^{16}O$	001–000, 020–000, 100–000
	$H^{12}C^{14}N$	1000–0000

(*continued on next page*)

Table 4 (*continued*)

Order	Isotopologue	Vibrational band
147	$^{12}C^{16}O_2$	13,302–00001, 14,402–01101, 21,102–00001, 21,103–00001, 21,112–00011, 21,113–11,101, 22,202–01101, 22,213–12,201, 23,302–02201, 24,402–03301, 25,502–04401, 30,002–01101, 30,003–01101, 31,102–02201, 31,102–10,001, 31,103–02201, 31,103–10,001, 31,103–10,002, 31,114–21,102, 32,202–11,101, 32,203–03301, 32,203–11,102, 33,302–12,201, 33,303–12,202, 40,002–11,101, 40,003–11,101, 40,003–11,102, 40,004–11,102, 41,102–20,001, 41,103–20,002, 41,104–12,202, 41,104–20,003
	$^{13}C^{16}O_2$	20,013–10,001, 21,102–00001, 21,113–11,101, 22,202–01101, 23,302–02201, 24,402–03301, 30,002–01101, 30,003–01101, 31,102–02201, 31,102–10,001, 31,103–02201, 31,103–10,002, 32,203–11,102, 40,004–11,102
	$^{16}O^{12}C^{18}O$	21,102–00001, 21,113–11,101, 22,202–01101, 23,302–02201, 30,002–01101, 31,102–10,001, 31,103–10,002
	$^{16}O^{12}C^{17}O$	21,102–00001, 22,202–01101, 30,002–01101, 30,003–01101
	$^{16}O^{13}C^{18}O$	20,013–10,001, 21,101–00001, 21,102–00001
	$H_2^{16}O$	001–000, 020–000, 100–000
	$HD^{16}O$	001–000
	$H^{12}C^{14}N$	1000–0000
148	$^{12}C^{16}O_2$	13,302–00001, 14,402–01101, 21,102–00001, 21,112–00011, 21,113–11,101, 22,202–01101, 22,213–12,201, 23,302–02201, 24,402–03301, 25,502–04401, 30,002–01101, 30,003–01101, 30,013–20,001, 30,014–20,002, 31,102–02201, 31,102–10,001, 31,103–02201, 31,103–10,002, 31,114–21,102, 32,202–11,101, 32,203–03301, 32,203–11,102, 33,302–12,201, 33,303–12,202, 4000–211,101, 40,003–11,101, 40,003–11,102, 40,004–11,102, 41,102–20,001, 41,103–20,002, 41,104–12,202, 41,104–20,003
	$^{13}C^{16}O_2$	14,412–04401, 15,512–05501, 20,013–10,001, 21,101–00001, 21,102–00001, 21,113–11,101, 22,202–01101, 23,302–02201, 24,402–03301, 30,002–01101, 30,003–01101, 31,102–02201, 31,102–10,001, 31,103–02201, 31,103–10,002, 32,203–11,102, 40,004–11,102
	$^{16}O^{12}C^{18}O$	20,013–10,001, 21,102–00001, 21,113–11,101, 22,202–01101, 23,302–02201, 30,002–01101, 31,102–10,001, 31,103–10,002
	$^{16}O^{12}C^{17}O$	21,102–00001, 22,202–01101, 30,002–01101, 30,003–01101
	$^{16}O^{13}C^{18}O$	13,312–03301, 20,013–10,001, 21,101–00001, 21,102–00001
	$H_2^{16}O$	001–000, 020–000, 100–000
	$HD^{16}O$	001–000
	$H^{12}C^{14}N$	1000–0000
149	$^{12}C^{16}O_2$	21,102–00001, 21,113–11,101, 22,202–01101, 23,302–02201, 30,002–01101, 30,003–01101, 31,102–10,001, 31,103–10,002, 32,203–11,102
	$^{13}C^{16}O_2$	20,013–10,001, 21,102–00001, 22,202–01101
	$^{16}O^{12}C^{18}O$	21,102–00001
	$^{16}O^{12}C^{17}O$	21,102–00001
	$H^{12}C^{14}N$	1000–0000
	$^{14}NH_3$	All
150	$^{12}C^{16}O_2$	13,301–00001, 13,302–00001, 14,401–01101, 15,512–05501, 16,612–06601, 20,013–10,001, 20,023–10,011, 21,102–00001, 21,112–00011, 21,113–11,101, 22,202–01101, 22,213–12,201, 23,302–02201, 24,402–03301, 25,502–04401, 30,002–01101, 30,003–01101, 30,013–20,001, 30,014–20,002, 31,102–02201, 31,102–10,001, 31,103–10,002, 31,114–21,102, 32,202–03301, 32,202–11,101, 32,203–11,102, 33,302–04401, 33,302–12,201, 33,303–12,202, 40,002–11,101, 40,003–11,102, 40,004–11,102, 41,102–20,001, 41,103–20,002, 41,104–20,003
	$^{13}C^{16}O_2$	10,022–00011, 11,112–01101, 11,122–01111, 12,212–02201, 12,222–02211, 13,301–00001, 13,312–03301, 14,412–04401, 15,512–05501, 20,013–02201, 20,013–10,001, 20,013–10,002, 20,023–10,012, 21,101–00001, 21,102–00001, 21,112–11,101, 21,113–11,101, 21,113–11,102, 22,201–01101, 22,202–01101, 22,212–12,201, 22,213–12,202, 23,302–02201, 23,312–13,301, 23,313–13,302, 24,402–03301, 30,002–01101, 30,013–20,001, 30,013–20,002, 30,014–20,003, 31,102–02201, 31,102–10,001, 31,102–10,002, 31,113–21,102, 31,114–21,103, 32,202–11,102, 40,002–03301
	$^{16}O^{12}C^{18}O$	14,412–04401, 20,013–10,001, 21,101–00001, 21,102–00001, 21,113–11,101, 22,202–01101, 23,302–02201, 30,002–01101, 31,102–10,001
	$^{16}O^{12}C^{17}O$	20,013–10,001, 21,102–00001, 22,202–01101, 30,002–01101
	$^{16}O^{13}C^{18}O$	10,012–00001, 10,022–00011, 11,112–01101, 12,212–02201, 13,312–03301, 20,012–10,001, 20,013–10,001, 20,013–10,002, 21,101–00001, 21,112–11,101, 21,113–11,102, 23,301–02201
	$^{12}C^{18}O_2$	12,212–02201
	$H_2^{16}O$	001–000, 100–000
	$H_2^{18}O$	100–000
	$HD^{16}O$	001–000
	$^{14}NH_3$	All
	$H^{12}C^{14}N$	100–000
151	$^{12}C^{16}O_2$	12,212–10,001, 13,301–00001, 13,312–03301, 14,401–01101, 14,412–04401, 15,512–05501, 16,612–06601, 20,013–02201, 20,013–10,001, 20,023–10,011, 21,101–00001, 21,102–00001, 21,113–11,101, 22,202–01101, 22,213–12,201, 22,213–12,202, 23,302–02201, 23,312–13,301, 23,313–13,302, 24,402–03301, 24,412–14,401, 24,413–14,402, 25,502–04401, 30,002–01101, 30,003–01101, 30,013–20,001, 30,014–20,002, 31,102–02201, 31,102–10,001, 31,103–10,002, 31,114 21,102, 31,114–21,103, 32,202–03301, 32,202–11,101, 32,203–11,102, 32,214–22,203, 33,302–04401, 33,302–12,201, 33,303–12,202, 33,314–23,303, 40,002–11,101, 40,003–11,102, 40,015–30,004, 41,102–04401, 41,102–12,201, 41,102–20,001, 41,103–12,202, 41,103–20,002, 41,115–31,104
	$^{13}C^{16}O_2$	10,012–00001, 10,022–00011, 11,112–01101, 11,122–01111, 12,212–02201, 12,212–10,002, 12,222–02211, 13,301–00001, 13,312–03301, 14,412–04401, 15,512–05501, 20,012–10,001, 20,013–02201, 20,013–10,001, 20,013–10,002, 20,023–10,012, 21,101–00001, 21,102–00001, 21,112–11,101, 21,113–11,101, 21,113–11,102, 22,201–01101, 22,202–01101, 22,212–12,201, 22,213–12,202, 23,301–02201, 23,302–02201, 23,312–13,301, 23,313–13,302, 30,001–01101, 30,002–01101, 30,012–20,001, 30,013–20,001, 30,013–20,002, 30,014–20,003, 31,101–10,001, 31,102–02201, 31,102–10,001, 31,102–10,002, 31,112–21,101, 31,113–21,102, 31,114–21,103, 32,202–11,102, 40,002–03301
	$^{16}O^{12}C^{18}O$	12,212–02201, 13,312–03301, 14,412–04401, 20,013–10,001, 21,101–00001, 21,102–00001, 21,112–11,101, 21,113–11,101, 21,113–11,102, 22,202–01101, 22,212–12,201, 22,213–12,202, 23,313–13,302, 30,002–01101, 30,014–20,003, 31,102–10,001, 31,114–21,103
	$^{16}O^{12}C^{17}O$	20,013–10,001, 21,101–00001, 21,102–00001, 22,202–01101, 30,002–01101
	$^{16}O^{13}C^{18}O$	10,012–00001, 10,022–00011, 11,112–01101, 12,212–02201, 13,312–03301, 20,012–10,001, 20,013–10,001, 20,013–10,002, 21,101–00001, 21,112–11,101, 21,113–11,102, 23,301–02201
	$^{16}O^{13}C^{17}O$	10,012–00001
	$^{12}C^{18}O_2$	10,012–00001, 11,112–01101, 12,212–02201, 13,312–03301, 20,012–10,001, 20,013–10,002, 21,112–11,101, 21,113–11,102, 23,301–02201
	$H_2^{16}O$	001–000, 100–000
	$H_2^{18}O$	100–000
	$HD^{16}O$	001–000
	$^{14}NH_3$	All
	$H^{12}C^{14}N$	100–000
152	$^{12}C^{16}O_2$	11,112–01101, 11,122–01111, 12,212–02201, 12,212–10,001, 12,222–02211, 13,301–00001, 13,312–03301, 13,322–03311, 14,401–01101, 14,412–04401, 15,512–05501, 16,612–06601, 20,013–02201, 20,013–10,001, 20,013–10,002, 20,023–10,011, 20,023–10,012, 21,101–00001, 21,102–00001, 21,111–00011, 21,112–11,101, 21,113–11,101, 21,113–11,102, 21,123–11,112, 22,202–01101, 22,212–12,201, 22,213–12,201, 22,213–12,202, 23,302–02201, 23,312–13,301, 23,313–13,302, 24,402–03301, 24,412–14,401, 24,413–14,402, 25,501–12,201, 25,502–04401,

(*continued on next page*)

Table 4 (*continued*)

Order	Isotopologue	Vibrational band
		25,513–15,502, 30,002–01101, 30,012–20,001, 30,013–20,001, 30,014–12,202, 30,014–20,002, 30,014–20,003, 31,102–02201, 31,102–10,001, 31,102–10,002, 31,103–10,002, 31,112–21,101, 31,113–21,102, 31,114–21,102, 31,114–21,103, 32,202–03301, 32,202–11,101, 32,202–11,102, 32,203–11,102, 32,212–22,201, 32,213–22,202, 32,214–22,203, 33,302–04401, 33,302–12,201, 33,303–12,202, 33,314–23,303, 40,002–11,101, 40,003–11,102, 40,015–30,004, 41,102–04401, 41,102–12,201, 41,102–20,001, 41,103–12,202, 41,103–20,002, 41,114–31,103, 41,115–31,104, 42,203–21,103
	$^{13}C^{16}O_2$	10,012–00001, 10,022–00011, 11,112–01101, 11,122–01111, 12,212–02201, 12,212–10,002, 12,222–02211, 13,301–00001, 13,312–03301, 14,412–04401, 15,512–05501, 20,012–10,001, 20,013–02201, 20,013–10,001, 20,013–10,002, 20,022–10,011, 20,023–10,012, 21,101–00001, 21,112–11,101, 21,113–11,102, 22,201–01101, 22,212–12,201, 22,213–12,202, 23,301–02201, 23,312–13,301, 23,313–13,302, 24,401–03301, 30,001–01101, 30,002–01101, 30,012–20,001, 30,013–20,001, 30,013–20,002, 30,014–20,003, 31,101–10,001, 31,102–02201, 31,102–10,001, 31,102–10,002, 31,112–21,101, 31,113–21,102, 31,114–21,103, 32,201–11,101, 32,202–11,102, 40,002–03301, 40,002–11,102
	$^{16}O^{12}C^{18}O$	10,012–00001, 10,022–00011, 11,112–01101, 11,122–01111, 12,212–02201, 13,312–03301, 14,412–04401, 20,012–10,001, 20,013–10,001, 20,013–10,002, 21,101–00001, 21,112–11,101, 21,113–11,101, 21,113–11,102, 22,201–01101, 22,212–12,201, 22,213–12,202, 23,301–02201, 23,313–13,302, 30,001–01101, 30,002–01101, 30,012–20,001, 30,013–20,002, 30,014–20,003, 31,113–21,102, 31,114–21,103
	$^{16}O^{12}C^{17}O$	12,212–02201, 13,312–03301, 14,412–04401, 20,013–10,001, 21,101–00001, 21,102–00001, 21,113–11,102, 22,202–01101, 22,213–12,202, 30,002–01101, 30,014–20,003
	$^{16}O^{13}C^{18}O$	10,012–00001, 10,022–00011, 11,112–01101, 12,212–02201, 13,312–03301, 20,012–10,001, 20,013–10,001, 20,013–10,002, 21,101–00001, 21,112–11,101, 21,113–11,102, 23,301–02201
	$^{16}O^{13}C^{17}O$	10,012–00001
	$^{12}C^{18}O_2$	10,012–00001, 11,112–01101, 12,212–02201, 13,312–03301, 20,012–10,001, 20,013–10,002, 21,112–11,101, 21,113–11,102, 23,301–02201
	$H_2^{16}O$	001–000, 100–000
	$H_2^{18}O$	100–000
	$HD^{16}O$	001–000
	$^{14}NH_3$	All
	$H^{12}C^{14}N$	100–000
	$^{12}C^{16}O_2$	02221–11,101, 10,011–00001, 10,022–11,101, 11,111–01101, 12,211–02201, 12,211–10,002, 13,311–03301, 14,411–04401, 15,511–05501, 16,611–06601, 20,011–02201, 20,011–10,001, 20,011–10,002, 20,012–10,002, 21,111–11,101, 21,111–11,102, 21,112–11,102, 22,211–12,201, 22,211–12,202, 22,212–12,202, 23,311–13,301, 23,312–13,302, 25,501–12,202, 30,011–20,001, 30,011–20,002, 30,012–20,003, 31,111–21,101, 31,112–21,103, 32,201–11,102, 40,001–11,102, 41,101–04401
	$^{13}C^{16}O_2$	00021–01101, 20,011–10,002, 21,111–11,102
169	$^{16}O^{12}C^{18}O$	20,011–10,002, 30,003–00001, 30,004–00001, 31,103–01101, 40,004–10,002
	$^{16}O^{12}C^{17}O$	10,011–00001, 11,111–01101, 12,211–02201, 13,311–03301, 20,011–10,002, 30,004–00001
	$H_2^{16}O$	001–000, 011–010, 020–000, 100–000, 011–000, 110–000
	$H_2^{18}O$	001–000, 100–000
	$H_2^{17}O$	001–000
	$HD^{16}O$	001–000
	$^{14}NH_3$	All
	$^{12}C^{16}O_2$	01121–10,001, 02221–11,101, 10,011–00001, 10,022–11,101, 11,111–01101, 12,211–02201, 12,211–10,002, 13,311–03301, 14,411–04401, 15,511–05501, 20,011–02201, 20,011–10,001, 20,011–10,002, 21,111–11,101, 21,111–11,102, 22,211–12,202, 30,011–20,002, 30,012–20,003, 31,112–21,103, 32,201–11,102, 40,001–11,102, 41,101–04401
	$^{13}C^{16}O_2$	00021–01101, 20,011–10,002, 21,111–11,102
	$^{16}O^{12}C^{18}O$	20,011–10,002, 30,003–00001, 30,004–00001, 31,103–01101, 40,004–10,002
	$^{16}O^{12}C^{17}O$	20,011–10,002, 30,003–00001, 30,004–00001
170	$H_2^{16}O$	001–000, 011–010, 020–000, 100–000
	$H_2^{18}O$	001–000, 100–000
	$H_2^{17}O$	001–000
	$HD^{16}O$	001–000
	$H^{19}F$	1–0
	$H_2^{32}S$	011–000, 110–000
	$^{14}NH_3$	All
	$^{12}C^{16}O_2$	00021–01101, 01121–02201, 01121–10,001, 02221–03301, 02221–11,101, 10,021–11,101, 10,022–11,101, 12,211–10,002, 20,011–02201, 20,011–10,002, 21,111–11,102, 22,211–12,202, 30,011–20,002, 30,012–20,003, 31,112–21,103
	$^{13}C^{16}O_2$	00021–01101, 01121–02201
	$^{16}O^{12}C^{18}O$	20,011–10,002, 30,003–00001, 31,103–01101, 40,004–10,002
	$^{16}O^{12}C^{17}O$	20,011–10,002, 30,003–00001
171	$H_2^{16}O$	001–000, 011–010, 020–000, 100–000
	$H_2^{18}O$	001–000, 100–000
	$H_2^{17}O$	001–000
	$HD^{16}O$	001–000
	$H_2^{32}S$	011–000, 110–000
	$^{14}NH_3$	All
	$^{12}C^{16}O_2$	00021–01101, 01121–02201, 01121–10,001, 02221–03301, 02221–11,101, 03321–04401, 03321–12,201, 10,021–11,101, 10,022–11,101, 10,022–11,102, 11,121–12,201, 11,121–20,001, 11,122–12,202, 11,122–20,002, 12,211–10,002, 20,011–10,002, 21,111–11,102, 22,211–12,202, 23,311–13,302, 30,011–20,002, 30,011–20,003, 30,012–20,003, 31,111–21,102, 31,112–21,103
	$^{13}C^{16}O_2$	00021–01101, 01121–02201, 01121–10,001, 01121–10,002, 02221–03301, 10,022–11,102
	$^{16}O^{12}C^{18}O$	00021–01101, 01121–10,001, 20,011–10,002, 21,111–11,102, 30,002–00001, 30,003–00001, 31,103–01101, 32,203–02201, 40,003–10,001, 40,003–10,002, 40,004–10,002
172	$^{16}O^{12}C^{17}O$	00021–01101, 20,011–10,002, 21,111–11,102, 30,003–00001, 31,103–01101
	$H_2^{16}O$	001–000, 011–010, 020–000, 100–000, 110–010
	$H_2^{18}O$	001–000, 100–000
	$H_2^{17}O$	001–000, 100–000
	$HD^{16}O$	001–000, 110–000
	$H_2^{32}S$	011–000, 110–000
	$^{14}NH_3$	All
190	$H_2^{16}O$	001–000, 100–000
	$HD^{16}O$	030–000, 110–000

(*continued on next page*)

Table 4 (*continued*)

Order	Isotopologue	Vibrational band
	$^{12}C^{16}O_2$	40,005–01101, 41,105–02201, 41,105–10,002
	$^{13}C^{16}O_2$	31,104–00001
	$^{16}O^{12}C^{18}O$	30,001–00001, 31,101–01101, 31,104–00001
	$^{16}O^{12}C^{17}O$	30,001–00001
	$^{12}C^{16}O$	2–0, 3–1
	$^{13}C^{16}O$	2–0
	$^{12}C^{18}O$	2–0
	$^{12}C^{17}O$	2–0
	$H^{19}F$	1–0
	$^{14}NH_3$	All
	$^{12}C^{16}O$	2–0, 3–1
	$^{13}C^{16}O$	2–0
	$^{12}C^{18}O$	2–0
	$^{12}C^{17}O$	2–0
	$H^{19}F$	1–0
191	$H_2^{16}O$	001–000, 030–000
	$HD^{16}O$	110–000
	$^{12}C^{16}O_2$	32,204–01101, 40,005–01101, 41,105–02201, 41,105–10,002
	$^{13}C^{16}O_2$	31,104–00001
	$^{16}O^{12}C^{18}O$	31,101–01101, 31,104–00001
	$^{16}O^{12}C^{17}O$	30,001–00001
	$^{14}NH_3$	All
	$^{12}C^{16}O$	2–0, 3–1
	$^{12}C^{17}O$	2–0
	$H^{19}F$	1–0
	$H_2^{16}O$	001–000, 030–000
192	$HD^{16}O$	110–000
	$^{12}C^{16}O_2$	31,104–00001, 32,204–01101, 33,304–02201, 40,005–01101, 41,105–02201, 41,105–10,002
	$^{13}C^{16}O_2$	31,104–00001
	$^{16}O^{12}C^{18}O$	31,104–00001
	$^{14}NH_3$	All

Appendix B. Application of the detection method to synthetic spectra

Similar to what was done in Mahieux et al. (2023a), to check the efficiency and robustness of the algorithm, we run tests on synthetic spectra that we build by choosing all atmospheric and instrumental parameters and then adding noise with equivalent SNR to the one of SOIR. We then run the LM algorithm to retrieve the parameters, compare the retrieved values to the known imposed ones, and run the detection criteria procedure. The synthetic spectra are computed at two typical altitudes – 65 and 80 km – with four typical SNRs equal to 500, 1000, 2000, and 3000. The atmospheric conditions are a temperature of 200 K and a pressure of 5.5 mbar, a CO_2 slant density of 1.7×10^{24} cm^{-2}, a slant path of 200 km for an altitude of 80 km, and a temperature of 230 K, a pressure of 65 mbar, CO_2 slant density of 1.7×10^{27} cm^{-2}, and slant path of 200 km for the altitude of 65 km. The VMRs of all the major species are taken as the values listed in the legend of Fig. 1. The VMRs of the minor species vary from 0.1 ppb to 10 ppm, varying by factors of 10. For all the positive detections, we checked that all the retrieved local number densities corresponded to the values used to build the spectra within the returned uncertainties.

Table 5
Detection of the targeted species listed in the first column for fits of synthetic spectra in the orders listed in the second column built with VMRs of the targeted species listed in the third column and SNRs corresponding to the third line. They are computed at altitudes of 65 and 80 km, see the second line of the table, for CO_2 slant densities of 1.7×10^{24} cm^{-2} and 1.7×10^{27} cm^{-2}, respectively, and VMRs of the other species as given in the legend of Fig. 1. Detections, corresponding to

✓

, are claimed for a reduction of the χ^2 of 5% (criterion a) and white-noise detection (criterion b), and fulfilling criterions c and d. No detections are indicated as

×

.

Species	Order	Initial VMR [ppm]	SNR							
			At 65 km				At 80 km			
			500	1000	2000	3000	500	1000	2000	3000
H_2CO	123	0.0001	✓	✓	✓	✓	×	×	×	×
		0.001	✓	✓	✓	✓	×	×	×	×
		0.01	✓	✓	✓	✓	×	✓	✓	✓
		0.1	✓	✓	✓	✓	✓	✓	✓	✓
		1	✓	✓	✓	✓	✓	✓	✓	✓
		10	✓	✓	✓	✓	✓	✓	✓	✓
	124	0.0001	✓	✓	✓	✓	×	×	×	×
		0.001	✓	✓	✓	✓	×	×	×	×
		0.01	✓	✓	✓	✓	×	✓	✓	✓
		0.1	✓	✓	✓	✓	✓	✓	✓	✓
		1	✓	✓	✓	✓	✓	✓	✓	✓
		10	✓	✓	✓	✓	✓	✓	✓	✓
	125	0.0001	✓	✓	✓	✓	×	×	×	×
		0.001	✓	✓	✓	✓	×	×	×	×
		0.01	✓	✓	✓	✓	×	✓	✓	✓
		0.1	✓	✓	✓	✓	✓	✓	✓	✓
		1	✓	✓	✓	✓	✓	✓	✓	✓
		10	✓	✓	✓	✓	✓	✓	✓	✓
	126	0.0001	✓	✓	✓	✓	×	×	×	×
		0.001	✓	✓	✓	✓	×	×	×	×
		0.01	✓	✓	✓	✓	×	×	✓	✓
		0.1	✓	✓	✓	✓	✓	✓	✓	✓
		1	✓	✓	✓	✓	✓	✓	✓	✓
		10	✓	✓	✓	✓	✓	✓	✓	✓
	127	0.0001	✓	✓	✓	✓	×	×	×	×
		0.001	✓	✓	✓	✓	×	×	×	×
		0.01	✓	✓	✓	✓	×	✓	✓	✓
		0.1	✓	✓	✓	✓	✓	✓	✓	✓
		1	✓	✓	✓	✓	✓	✓	✓	✓
		10	✓	✓	✓	✓	✓	✓	✓	✓
	128	0.0001	✓	✓	✓	✓	×	×	×	×
		0.001	✓	✓	✓	✓	×	×	×	×
		0.01	✓	✓	✓	✓	×	✓	✓	✓
		0.1	✓	✓	✓	✓	✓	✓	✓	✓
		1	✓	✓	✓	✓	✓	✓	✓	✓
		10	✓	✓	✓	✓	✓	✓	✓	✓

O_3	134	0.0001	×	×	×	×	×	×	×	×
		0.001	×	×	✓	✓	×	×	×	×
		0.01	✓	✓	✓	✓	×	×	×	×
		0.1	✓	✓	✓	✓	×	×	×	×
		1	✓	✓	✓	✓	×	×	✓	✓
		10	✓	✓	✓	✓	✓	✓	✓	✓
	135	0.0001	×	×	×	×	×	×	×	×
		0.001	×	✓	✓	✓	×	×	×	×
		0.01	✓	✓	✓	✓	×	×	×	×
		0.1	✓	✓	✓	✓	×	×	×	✓
		1	✓	✓	✓	✓	✓	✓	✓	✓
		10	✓	✓	✓	✓	✓	✓	✓	✓
NH_3	150	0.0001	×	×	×	×	×	×	×	×
		0.001	×	×	×	×	×	×	×	×
		0.01	×	×	×	×	×	×	×	×
		0.1	✓	✓	✓	✓	×	×	✓	✓
		1	✓	✓	✓	✓	✓	✓	✓	✓
		10	✓	✓	✓	✓	✓	✓	✓	✓
	151	0.0001	×	×	×	×	×	×	×	×
		0.001	×	×	×	×	×	×	×	×
		0.01	×	×	×	×	×	×	×	×
		0.1	✓	✓	✓	✓	×	✓	✓	✓
		1	✓	✓	✓	✓	✓	✓	✓	✓
		10	✓	✓	✓	✓	✓	✓	✓	✓
	152	0.0001	×	×	×	×	×	×	×	×
		0.001	×	×	×	×	×	×	×	×
		0.01	×	×	×	×	×	×	×	×
		0.1	✓	✓	✓	✓	×	×	✓	✓
		1	✓	✓	✓	✓	✓	✓	✓	✓
		10	✓	✓	✓	✓	✓	✓	✓	✓
	191	0.0001	×	×	×	×	×	×	×	×
		0.001	×	✓	✓	✓	×	×	×	×
		0.01	✓	✓	✓	✓	×	×	×	×
		0.1	✓	✓	✓	✓	×	×	×	×
		1	✓	✓	✓	✓	×	✓	✓	✓
		10	✓	✓	✓	✓	✓	✓	✓	✓
	192	0.0001	×	×	×	×	×	×	×	×
		0.001	×	✓	✓	✓	×	×	×	×
		0.01	✓	✓	✓	✓	×	×	×	×
		0.1	✓	✓	✓	✓	×	×	×	×
		1	✓	✓	✓	✓	×	×	×	✓
		10	✓	✓	✓	✓	✓	✓	✓	✓

HCN	145	0.0001	×	×	×	✓	×	×	×	×
		0.001	✓	✓	✓	✓	×	×	×	×
		0.01	✓	✓	✓	✓	×	×	×	✓
		0.1	✓	✓	✓	✓	✓	✓	✓	✓
		1	✓	✓	✓	✓	✓	✓	✓	✓
		10	✓	✓	✓	✓	✓	✓	✓	✓
	146	0.0001	✓	✓	✓	✓	×	×	×	×
		0.001	✓	✓	✓	✓	×	×	×	×
		0.01	✓	✓	✓	✓	×	✓	✓	✓
		0.1	✓	✓	✓	✓	✓	✓	✓	✓
		1	✓	✓	✓	✓	✓	✓	✓	✓
		10	✓	✓	✓	✓	✓	✓	✓	✓
	147	0.0001	✓	✓	✓	✓	×	×	×	×
		0.001	✓	✓	✓	✓	×	×	×	✓
		0.01	✓	✓	✓	✓	×	✓	✓	✓
		0.1	✓	✓	✓	✓	✓	✓	✓	✓
		1	✓	✓	✓	✓	✓	✓	✓	✓
		10	✓	✓	✓	✓	✓	✓	✓	✓
	148	0.0001	×	×	×	×	×	×	×	×
		0.001	×	×	×	×	×	×	×	×
		0.01	×	✓	✓	✓	×	✓	✓	✓
		0.1	✓	✓	✓	✓	✓	✓	✓	✓
		1	✓	✓	✓	✓	✓	✓	✓	✓
		10	✓	✓	✓	✓	✓	✓	✓	✓
	149	0.0001	✓	✓	✓	✓	×	×	×	×
		0.001	✓	✓	✓	✓	×	×	×	×
		0.01	✓	✓	✓	✓	×	×	×	×
		0.1	✓	✓	✓	✓	×	×	×	×
		1	✓	✓	✓	✓	✓	✓	✓	✓
		10	✓	✓	✓	✓	✓	✓	✓	✓
N_2O	113	0.0001	×	✓	✓	✓	×	×	×	×
		0.001	✓	✓	✓	✓	×	×	×	×
		0.01	✓	✓	✓	✓	×	×	×	×
		0.1	✓	✓	✓	✓	×	✓	✓	✓
		1	✓	✓	✓	✓	✓	✓	✓	✓
		10	✓	✓	✓	✓	✓	✓	✓	✓

	114	0.0001	×	✓	✓	✓	×	×	×	×
		0.001	✓	✓	✓	✓	×	×	×	×
		0.01	✓	✓	✓	✓	×	×	×	×
		0.1	✓	✓	✓	✓	✓	✓	✓	✓
		1	✓	✓	✓	✓	✓	✓	✓	✓
		10	✓	✓	✓	✓	✓	✓	✓	✓
	115	0.0001	×	×	×	×	×	×	×	×
		0.001	✓	✓	✓	✓	×	×	×	×
		0.01	✓	✓	✓	✓	×	×	×	×
		0.1	✓	✓	✓	✓	✓	✓	✓	✓
		1	✓	✓	✓	✓	✓	✓	✓	✓
		10	✓	✓	✓	✓	✓	✓	✓	✓
NO_2	129	0.0001	✓	✓	✓	✓	×	×	×	×
		0.001	✓	✓	✓	✓	×	×	×	×
		0.01	✓	✓	✓	✓	×	×	×	×
		0.1	✓	✓	✓	✓	✓	✓	✓	✓
		1	✓	✓	✓	✓	✓	✓	✓	✓
		10	✓	✓	✓	✓	✓	✓	✓	✓
	130	0.0001	✓	✓	✓	✓	×	×	×	×
		0.001	✓	✓	✓	✓	×	×	×	×
		0.01	✓	✓	✓	✓	×	×	×	✓
		0.1	✓	✓	✓	✓	✓	✓	✓	✓
		1	✓	✓	✓	✓	✓	✓	✓	✓
		10	✓	✓	✓	✓	✓	✓	✓	✓
NO	169	0.0001	×	×	×	×	×	×	×	×
		0.001	×	×	×	×	×	×	×	×
		0.01	×	×	×	×	×	×	×	×
		0.1	×	×	×	×	×	×	×	×
		1	×	×	×	×	×	×	×	×
		10	×	×	×	×	×	×	✓	✓
	170	0.0001	×	×	×	×	×	×	×	×
		0.001	×	×	×	×	×	×	×	×
		0.01	×	×	×	×	×	×	×	×
		0.1	×	×	×	×	×	×	×	×
		1	×	×	×	×	×	×	×	×
		10	×	×	×	×	×	×	✓	✓
	171	0.0001	×	×	×	×	×	×	×	×
		0.001	×	×	×	×	×	×	×	×

		0.01	×	×	×	×	×	×	×	×
		0.1	×	×	×	✓	×	×	×	×
		1	×	✓	✓	✓	×	×	×	×
		10	✓	✓	✓	✓	×	×	×	×
	172	0.0001	×	×	×	×	×	×	×	×
		0.001	×	×	×	×	×	×	×	×
		0.01	×	×	×	×	×	×	×	×
		0.1	×	×	×	×	×	×	×	×
		1	×	×	×	×	×	×	×	×
		10	×	✓	✓	✓	×	×	×	×
	173	0.0001	×	×	×	×	×	×	×	×
		0.001	×	×	×	×	×	×	×	×
		0.01	×	×	×	×	×	×	×	×
		0.1	×	×	×	×	×	×	×	×
		1	×	×	×	×	×	×	×	×
		10	×	✓	✓	✓	×	×	×	×
HO_2	150	0.0001	×	×	×	×	✓	✓	✓	✓
		0.001	×	✓	✓	✓	✓	✓	✓	✓
		0.01	✓	✓	✓	✓	✓	✓	✓	✓
		0.1	✓	✓	✓	✓	✓	✓	✓	✓
		1	✓	✓	✓	✓	✓	✓	✓	✓
		10	✓	✓	✓	✓	×	✓	✓	✓
	151	0.0001	×	×	×	×	✓	✓	✓	✓
		0.001	×	✓	✓	✓	✓	✓	✓	✓
		0.01	✓	✓	✓	✓	✓	✓	✓	✓
		0.1	✓	✓	✓	✓	✓	✓	✓	✓
		1	✓	✓	✓	✓	✓	✓	✓	✓
		10	✓	✓	✓	✓	✓	✓	✓	✓
	152	0.0001	×	×	×	×	✓	✓	✓	✓
		0.001	×	✓	✓	✓	✓	✓	✓	✓
		0.01	✓	✓	✓	✓	✓	✓	✓	✓
		0.1	✓	✓	✓	✓	✓	✓	✓	✓
		1	✓	✓	✓	✓	✓	✓	✓	✓
		10	✓	✓	✓	✓	✓	✓	✓	✓

This exercise shows that all the species should be detectable, at least in some orders, for all SOIR typical SNRs and VMRs down to 0.1 ppb. While doing this exercise, we checked that for all positive detections, the retrieved number density was always equal to the a priori density used to build the synthetic spectra within the uncertainties returned by the LM algorithm.

We note that the upper limit number densities and VMRs obtained by considering the synthetic spectra discussed in this Section are of the same order of magnitude as the ones discussed in the main text body.

References

Bains, W., et al., 2021. Phosphine on Venus cannot be explained by conventional processes. Astrobiology. 21, 1277–1304.

Belyaev, D.A., et al., 2017. Night side distribution of SO 2 content in Venus' upper mesosphere. Icarus. 294, 58–71.

Bertaux, J.L., et al., 2007. SPICAV on Venus Express: three spectrometers to study the global structure and composition of the Venus atmosphere. Planet. Space Sci. 55, 1673–1700.

Chamberlain, S., et al., 2020. SOIR/VEx observations of water vapor at the terminator in the Venus mesosphere. Icarus. 346, 113819.

Cleland, C.E., Rimmer, P.B., 2022. Ammonia and phosphine in the clouds of Venus as potentially biological anomalies. Aerospace. 9, 752.

Clements, D.L., 2022. Venus, phosphine and the possibility of life. Contemp. Phys. 63, 180–199.

Encrenaz, T., et al., 2020. A stringent upper limit of the PH_3 abundance at the cloud top of Venus. Astron. Astrophys. 643.

Evdokimova, D., et al., 2021. The spatial and temporal distribution of nighttime ozone and sulfur dioxide in the Venus mesosphere as deduced from SPICAV UV stellar occultations. J. Geophys. Res. 126 e2020JE006625.

Fedorova, A., et al., 2008. HDO and H_2O vertical distributions and isotopic ratio in the Venus mesosphere by Solar Occultation at Infrared spectrometer onboard Venus Express. J. Geophys. Res. 113, E00B22.

Gilli, G., et al., 2015. Carbon monoxide and temperature in the upper atmosphere of Venus from VIRTIS/Venus Express non-LTE limb measurements. Icarus. 248, 478–498.

Gordon, I.E., et al., 2017. The HITRAN2016 molecular spectroscopic database. J. Quant. Spectrosc. Radiat. Transf. 203, 3–69.

Greaves, J.S., et al., 2021. Phosphine gas in the cloud decks of Venus. Nat. Astron. 5, 655–664.

Greaves, J., Petkowski, J.J., Richards, A.M.S., et al., 2023. Comment on "Phosphine in the Venusian Atmosphere: A Strict Upper Limit from SOFIA GREAT Observations" by Cordiner et al. ESS Open Archive.

Gröller, H., et al., 2018. MAVEN/IUVS stellar occultation measurements of Mars atmospheric structure and composition. J. Geophys. Res.: Planets. 123, 1449–1483.

Häusler, B., et al., 2006. Radio science investigations by VeRa onboard the Venus Express spacecraft. Planet. Space Sci. 54, 1315–1335.

Hedin, A.E., Niemann, H.B., Kasprzak, W.T., 1983. Global empirical model of the Venus thermosphere. J. Geophys. Res. 88, 73–83.

IUPAC, 2008. IUPAC Compendium of Chemical Terminology (IUPAC).

Khatuntsev, I., et al., 2013. Cloud level winds from the Venus Express Monitoring Camera imaging. Icarus. 226, 140–158.

Krasnopolsky, V.A., 2006. A sensitive search for nitric oxide in the lower atmospheres of Venus and Mars: detection on Venus and upper limit for Mars. Icarus. 182, 80–91.

Krasnopolsky, V., 2012. Observation of DCl and upper limit to NH_3 on Venus. Icarus. 219, 244–249.

Krasnopolsky, V., Parshev, V.A., 1983. Photochemistry of the Venus atmosphere. In: Hunten, D.M., Colin, L., Donahue, T.M., Moroz, L.V. (Eds.), Venus. University of Arizona Press, Tucson, pp. 431–458.

Limaye, S., et al., 2017. The thermal structure of the Venus atmosphere: intercomparison of Venus express and ground based observations of vertical temperature and density profiles. Icarus. 294, 124–155.

Limaye, S.S., Grassi, D., Mahieux, A., Migliorini, A., Tellmann, S., Titov, D., 2018. Venus atmospheric thermal structure and radiative balance. Space Sci. Rev. 214, 102.

Mahieux, A., et al., 2008. In-flight performance and calibration of SPICAV/SOIR on-board Venus Express. Appl. Optics 47, 2252–2265.

Mahieux, A., Wilquet, V., Drummond, R., Belyaev, D., Fedorova, A., Vandaele, A.C., 2009. A new method for determining the transfer function of an acousto optical tunable filter. Opt. Express 17, 2005–2014.

Mahieux, A., et al., 2015a. Update of the Venus density and temperature profiles at high altitude measured by SOIR on board Venus Express. Planet. Space Sci. 113-114, 309–320.

Mahieux, A., et al., 2015b. Venus mesospheric sulfur dioxide measurement retrieved from SOIR on board Venus Express. Planet. Space Sci. 113-114, 193–204.
Mahieux, A., Wilquet, V., Vandaele, A.C., Robert, S., Drummond, R., Bertaux, J.L., 2015c. Hydrogen halides measurements in the Venus upper atmosphere retrieved from SOIR on board Venus Express. Planet. Space Sci. 113-114, 264–274.
Mahieux, A., et al., 2023a. Update on SO2, detection of OCS, CS, CS2, and SO3, and upper limits of H2S and HOCl in the Venus mesosphere using SOIR on board Venus Express. Icarus. 399, 115556.
Mahieux, A., Robert, S., Piccialli, A., Trompet, L., Vandaele, A.C., 2023b. The SOIR/Venus Express species concentration and temperature database: CO2, CO, H2O, HDO, H35Cl, H37Cl, HF individual and mean profiles. Icarus. 115713.
Marcq, E., Mills, F.P., Parkinson, C.D., Vandaele, A.C., 2018. Composition and chemistry of the neutral atmosphere of Venus. Space Sci. Rev. 214 article 10.
Marcq, E., et al., 2019. Discovery of cloud top ozone on Venus. Icarus. 319, 491–498.
Marcq, E., et al., 2020. Climatology of SO$_2$ and UV absorber at Venus' cloud top from SPICAV-UV nadir dataset. Icarus. 335.
Markiewicz, W.J., et al., 2007. Venus monitoring camera for Venus Express. Planet. Space Sci. 55, 1701–1711.
Mills, F.P., Allen, M., 2007. A review of selected issues concerning the chemistry in Venus' middle atmosphere. Planet. Space Sci. 55, 1729–1740.
Mills, F.P., Esposito, L.W., Yung, Y.L., 2007. Atmospheric composition, chemistry and clouds. Geophys. Monogr. Ser. 176, 73–100.
Mogul, R., Limaye, S.S., Way, M.J., Cordova, J.A., 2021. Venus' mass spectra show signs of disequilibria in the middle clouds. Geophys. Res. Lett. 48 e2020GL091327.
Montmessin, F., et al., 2011. A layer of ozone detected in the nightside upper atmosphere of Venus. Icarus. 216, 82–85.
Müller-Wodarg, I.C.F., Bruinsma, S., Marty, J.-C., Svedhem, H., 2016. In situ observations of waves in Venus's polar lower thermosphere with Venus Express aerobraking. Nat. Phys. 12, 767–771.
Nna Mvondo, D., Navarro-Gonzalez, R., McKay, C.P., Coll, P., Raulin, F., 2001. Production of nitrogen oxides by lightning and coronae discharges in simulated early Earth, Venus and Mars environments. Adv. Space Res. 27, 217–223.
Oschlisniok, J., et al., 2021. Sulfuric acid vapor and sulfur dioxide in the atmosphere of Venus as observed by the Venus Express radio science experiment VeRa. Icarus. 362, 114405.
Otroshchenko, V.A., Surkov, Y.A., 1974. The possibility of organic molecule formation in the Venus atmosphere. In: Oró, J., Miller, S.L., Ponnamperuma, C., Young, R.S. (Eds.), Cosmochemical Evolution and the Origins of Life. Springer Netherlands, Dordrecht, pp. 487–490.
Piccialli, A., et al., 2012. Dynamical properties of the Venus mesosphere from the radio-occultation experiment VeRa onboard Venus Express. Icarus. 217, 669–681.
Piccialli, A., et al., 2014. High latitude gravity waves at the Venus cloud tops as observed by the Venus Monitoring Camera on board Venus Express. Icarus. 227, 94.
Piccialli, A., et al., 2015. Thermal structure of Venus upper aymosphere measured by stellar occultations with SPICAV/Venus Express. Planet. Space Sci. 113-114, 321–335.
Piccioni, G., et al., 2007. VIRTIS: The Visible and Infrared Thermal Imaging Spectrometer. ESA Special Publication, p. SP 1295.
Piccioni, G., et al., 2008. First detection of hydroxyl in the atmosphere of Venus. Astron. Astrophys. 483, L29–L33.
Royer, E.M., Montmessin, F., Marcq, E., 2016. Variability of the nitric oxide nightglow at Venus during solar minimum. J. Geophys. Res. Planets. 121, 846–853.
Spacek, J., Rimmer, P., Cady, S., Owens, G., Sharma, D., Benner, S.A., 2023. Organics produced in the clouds of Venus resemble the spectrum of the unknown absorber. In: LPI Contrib. 2807, p. 8060.
Surkov, Y.A., Andrejchikov, B.M., Kalinkina, O.M., 1973. On the content of ammonia in the Venus atmosphere based on data obtained from Venera 8 automatic station. Akademiia Nauk SSSR Doklady. 213.
Tellmann, S., et al., 2012. Small-scale temperature fluctuations seen by the VeRa Radio Science Experiment on Venus Express. Icarus. 221, 471–480.
Titov, D.V., et al., 2006a. Venus Express science planning. Planet. Space Sci. 54, 1279–1297.
Titov, D.V., et al., 2006b. Venus Express: scientific goals, instrumentation and scenario of the mission. Cosm. Res. 44, 334–348.
Trompet, L., et al., 2016. Improved algorithm for the transmittance estimation of spectra obtained with SOIR/Venus Express. Appl. Optics 55, 9275–9281.
Trompet, L., et al., 2018. Description, accessibility and usage of SOIR/Venus Express atmospheric profiles of Venus distributed in VESPA (Virtual European Solar and Planetary Access). Planet. Space Sci. 150, 60–64.
Trompet, L., et al., 2023. Carbon dioxide retrievals from NOMAD-SO on ESA's ExoMars Trace Gas Orbiter and temperature profiles retrievals with the hydrostatic equilibrium equation: 1. Description of the method. J. Geophys. Res.: Planets 128, e2022JE007277.
Trompet, L., Robert, S., Mahieux, A., Schmidt, F., Erwin, J., Vandaele, A.C., 2021. Phosphine in Venus' atmosphere: detection attempts and upper limits above the cloud top assessed from the SOIR/VEx spectra. A&A. 645, L4.
Vandaele, A.C., et al., 2013. Improved calibration of SOIR/Venus Express spectra. Opt. Express 21, 21148.
Vandaele, A.C., Mahieux, A., Robert, S., Drummond, R., Wilquet, V., Bertaux, J.L., 2015. Carbon monoxide short term variability observed on Venus with SOIR/VEX. Planet. Space Sci. 113-114, 237–255.
Vandaele, A.C., et al., 2016a. Contribution from SOIR/VEX to the updated Venus International Reference Atmosphere (VIRA). Adv. Space Res. 57, 443–458.
Vandaele, A.C., et al., 2016b. Carbon monoxide observed in Venus' atmosphere with SOIR/VEx. Icarus. 272, 48–59.
Villanueva, G.L., et al., 2021. No evidence of phosphine in the atmosphere of Venus from independent analyses. Nat. Astron. 5, 631–635.
Wildt, R., 1940. On the possible existence of formaldehyde in the atmosphere of Venus. Astrophys. J. 92, 247.
Zasova, L.V., Moroz, V.I., Linkin, V.M., Khatountsev, I.A., Maiorov, B.S., 2006. Structure of the Venusian atmosphere from surface up to 100 km. Cosmic Res. 44, 364–383.
Zhang, X., Liang, M., Mills, F., Belyaev, D., Yung, Y., 2012. Sulfur chemistry in the middle atmosphere of Venus. Icarus. 217, 714–739.
Zolotov, M.Y., 1991. Redox conditions of the near surface atmosphere of Venus. II. Equilibrium and disequilibrium models. In: Lunar and Planetary Science Conference, pp. 1573.